# All-sky search in early O3 LIGO data for continuous gravitational-wave signals from unknown neutron stars in binary systems

R. Abbott *et al.*[*]

(The LIGO Scientific Collaboration and the Virgo Collaboration)

Rapidly spinning neutron stars are promising sources of continuous gravitational waves. Detecting such a signal would allow probing of the physical properties of matter under extreme conditions. A significant fraction of the known pulsar population belongs to binary systems. Searching for unknown neutron stars in binary systems requires specialized algorithms to address unknown orbital frequency modulations. We present a search for continuous gravitational waves emitted by neutron stars in binary systems in early data from the third observing run of the Advanced LIGO and Advanced Virgo detectors using the semicoherent, GPU-accelerated, BinarySkyHough pipeline. The search analyzes the most sensitive frequency band of the LIGO detectors, 50–300 Hz. Binary orbital parameters are split into four regions, comprising orbital periods of three to 45 days and projected semimajor axes of two to 40 light seconds. No detections are reported. We estimate the sensitivity of the search using simulated continuous wave signals, achieving the most sensitive results to date across the analyzed parameter space.

## I. INTRODUCTION

Continuous gravitational waves (CWs) are a long-lasting form of gravitational radiation. For ground-based interferometric detectors, the canonical sources are rapidly spinning neutron stars (NSs) sustaining a quadrupolar deformation. Several emission mechanisms have been proposed, such as crustal deformations, r modes, or free precession (see [1] for a recent review). Detecting CWs would probe the physics of such compact objects, leading us to a better understanding of the equation of state of matter under extreme conditions. More exotic types of CW sources are also theorized, such as boson clouds around spinning black holes [2].

Every CW search method assumes certain information about the intended sources. All-sky searches, such as the one reported in this paper, impose the least amount of constraints on the CW emission. The latest results obtained by the LIGO-Virgo collaboration using Advanced LIGO [3] and Advanced Virgo [4] data, covering targeted (known pulsars), directed (known sky locations), and all-sky searches, can be found in [5–10].

All-sky searches require highly efficient analysis methods because they must account for a Doppler modulation due to the Earth's movement with respect to the solar system barycenter (SSB), an effect that depends on sky position. In principle, one can construct a search pipeline using fully coherent matched filtering; for wide parameter space searches, however, such an approach quickly

becomes computationally unaffordable [11]. As a result, semicoherent methods are used, splitting the data stream into smaller time segments that can be coherently analyzed. Then, per-segment results are combined according to the expected frequency evolution of the template under analysis. This method reduces the computational cost of a search while achieving a reasonable sensitivity.

Only a small fraction of the expected population of galactic NSs has been detected electromagnetically [12]. Through gravitational waves, we could access these unknown populations of NSs. About half of the NSs detected using electromagnetic means within the most sensitive frequency band of current ground-based detectors are part of a binary system [13,14]. Searches for CWs from this class of NSs pose an additional, substantial computational challenge compared to standard all-sky searches that target isolated NSs because additional unknown binary orbital parameters increase the search parameter space dimensionality. As a result, one must use specialized methods in order to search for this type of signal.

We present an all-sky search for CWs produced by NSs in binary systems using the semicoherent BinarySkyHough pipeline [13]. It builds upon SkyHough [15], inheriting its characteristic noise robustness and computational efficiency, and uses graphics processing units (GPUs) to speed up the core part of the search. The concept of BinarySkyHough is to compute search statistics over the parameter space and to use those statistics to rank the interesting regions for subsequent follow-up using more sensitive, computationally demanding techniques. This balance between sensitivity and computational cost has

---

proven effective in previous searches of the LIGO O2 observing run data using both the isolated SkyHough [8] and BinarySkyHough [16] flavors of this pipeline.

In Sec. II, we introduce the signal model; Sec. III describes the early third observing run of the Advanced LIGO and Advanced Virgo detectors; Sec. IV briefly describes the main analysis pipeline; Sec. V introduces the first post processing stage; and, in Sec. VI, we estimate the sensitivity of this search. In Sec. VII, we further analyze the most significant outliers and rule them out as nonastrophysical candidates. We present our conclusions in Sec. VIII.

## II. SIGNAL MODEL

A nonaxisymmetric neutron star spinning about one of its principal axes is expected to emit gravitational waves at twice its rotation frequency $f_0 = 2f_{\rm rot}$ with a strain amplitude given by [17]

$$h(t) = h_0 \left[ F_+(t; \psi, \hat{n}) \frac{1 + \cos \iota}{2} \cos \phi(t) \right.$$
$$\left. + F_\times(t; \psi, \hat{n}) \cos \iota \sin \phi(t) \right], \qquad (1)$$

where $F_{+,\times}$ are the antenna patterns of the interferometric detectors, depending on the polarization angle $\psi$ and the sky position $\hat{n}$ of the source; $h_0$ and $\cos \iota$ are the characteristic CW amplitude and the cosine of the inclination of the source with respect to the line of sight, respectively; and $\phi(t)$ represents the phase of the gravitational wave signal.

The CW amplitude $h_0$ can be expressed in terms of the physical properties of the source once an emission mechanism has been assumed. The three principal moments of inertia of a nonaxisymmetric NS are given by $I_x, I_y, I_z$, and the equatorial ellipticity is given by $\epsilon = |I_x - I_y|/I_z$, assuming the spin axis is aligned with $I_z$. The gravitational wave amplitude can be expressed as

$$h_0 = \frac{4\pi^2 G}{c^4} \frac{I_z \epsilon}{d} f_0^2, \qquad (2)$$

where $d$ denotes the distance to the source from the detector, $f_0$ the gravitational wave frequency, and $G$ and $c$, respectively, refer to the gravitational constant and the speed of light. We can further relate this quantity to the mass quadrupole $Q_{22}$ of the star through the equatorial ellipticity,

$$\epsilon = \sqrt{\frac{8\pi}{15}} \frac{Q_{22}}{I_z}. \qquad (3)$$

We can describe the signal phase via Taylor expansion with respect to a fiducial starting time $\tau_0$ in the source frame,

$$\phi(\tau) = \phi_0 + 2\pi [f_0 \cdot (\tau - \tau_0) + \ldots], \qquad (4)$$

where $\tau$ is the proper source frame time, and $\phi_0$ represents the initial phase at $\tau_0$. The number of higher order terms to include in this expansion depends on the population of NSs under consideration. After analyzing the ATNF pulsar catalog [14], it was argued in [13] that searching for NSs in binary systems need not take into account any spin-down parameters when using datasets lasting for less than a few years. As we will discuss in Sec. VIII, this search remains sensitive to signals up to a certain spin-down value, but there is an implicit limit on the astrophysical reach.

Because of the relative motion of the detector around the SSB and the relative motion of the source around the binary system barycenter (BSB), the phase as measured by the detector at time $t$ is Doppler modulated according to the timing relation,

$$\tau + a_p \sin \left[ \Omega(\tau - \tau_{\rm asc}) \right] = t + \frac{\vec{r}(t) \cdot \hat{n}}{c} - \frac{d}{c}, \qquad (5)$$

where $a_p$ represents the semimajor axis of the binary orbit projected onto the line of sight (measured in light seconds), $\Omega$ represents the orbital frequency of the source, $\tau_{\rm asc}$ represents the time of passage through the ascending node as measured from the source frame, and $\vec{r}$ represents the position of the detector in the SSB. In order to derive this expression, we assumed circular, Keplerian orbits; the search remains sensitive, however, to signals from sources in binary systems up to a certain eccentricity as discussed in Section VII A and [13].

We define a *template* as $\lambda = \{f_0, \hat{n}, a_p, \Omega, t_{\rm asc}\}$. The parameter space (*i.e.*, the set of all templates searched) will be denoted as $\mathbb{P}$. The orbital period is related to the orbital angular frequency by $P = 2\pi/\Omega$.

We refer the reader to [18] for a complete derivation of Eq. (5) and a discussion about how to express Eq. (4) in the detector frame. The gravitational wave frequency evolution associated to a template $\lambda$ as measured from the detector frame is thus

$$f_\lambda(t) = f_0 \cdot \left( 1 + \frac{\vec{v}(t) \cdot \hat{n}}{c} - a_p \Omega \cos \left[ \Omega(t - t_{\rm asc}) \right] \right), \qquad (6)$$

where $\vec{v}(t)$ refers to the detector velocity, and $t_{\rm asc}$ is akin to $\tau_{\rm asc}$ measured from the detector frame. We choose the initial phase $t_{\rm asc}$ to be located within the range $[t_{\rm mid} - \frac{P}{2}, t_{\rm mid} + \frac{P}{2}]$, where $t_{\rm mid}$ represents the mean time between the start and the end of the run measured in GPS seconds.

## III. DATA USED

The first part of the third observing run of the Advanced LIGO and Advanced Virgo detectors (O3a) comprises six months of data collected from April 1, 2019 at 15:00 UTC

to October 1, 2019 at 15:00 UTC. Data was taken by the Advanced LIGO detectors, located in Hanford (Washington, USA, designated H1) and Livingston (Lousiana, USA, designated L1), together with the Advanced Virgo detector, located in Cascina (Pisa, Italy). We did not make use of Advanced Virgo data because of an unfavorable trade-off between computing cost and expected sensitivity improvement of the search. The detector duty factor (the fraction of the run when the detector is collecting observational-quality data) was 71.2% for H1 and 75.8% for L1. The implementation of instrumental upgrades has allowed the detectors to improve their overall sensitivities with respect to the previous observing run (O2) [19].

For the duration of the run, several artificial signals were injected into both detectors in order to calibrate and monitor their performance. *Calibration lines* are artificial monochromatic signals, injected at different frequencies in each detector to avoid coherent artifacts. They are used to monitor time-varying detector operating parameters. *Hardware injections*, on the other hand, are artificial quasimonochromatic signals consistently injected into both detectors in order to mimic the effects of an actual CW signal present in both detectors. They are used to verify expected detector response and characterize calibrated data [20]. Both of these artificial signals may interfere with CW searches in general, showing up as significant candidates due to their high strength in the detector spectrum. Spectral artifacts in detector data can be produced by environmental or instrumental noise and also interfere with CW searches [21].

The search was performed using short Fourier transforms (SFTs) created from the C00 (initial calibration version) time-domain observing-quality strain data [22]. These SFTs were extracted from short Fourier data base (SFDB) data [23], which incorporates a time-domain cleaning procedure to avoid noise-floor degradation due to glitches and other forms of transient noise. Every SFT lies completely within observing-quality data. Fourier transforms were computed using a Tukey-windowed baseline of $T_{\mathrm{SFT}} = 1024$ s, with tapering parameter $\beta_{\mathrm{Tukey}} = 0.5$ and a 50% overlap. These values are collected in Table I.

Following the same procedure used in the O2 SkyHough search [8], SFT data are split into two datasets to be used in two different stages of the search. The first dataset, which we refer to as *nonoverlapping*, leaves out overlapping SFTs (*i.e.*, every SFT starts at the end of the previous one). The second dataset, which we refer to as *overlapping*, contains all of the SFTs. Using the nonoverlapping set for the first stage of the analysis reduces the computational cost of the search at a manageable loss in sensitivity. Table II lists the number of SFTs in each of the datasets. Datasets contain SFTs from *both* LIGO detectors (*i.e.*, we perform a *multidetector* search [13]).

TABLE I. Miscellaneous parameters used in the search. $T_{\mathrm{SFT}}$ denotes the time span employed to compute short Fourier transforms (SFTs). $\beta_{\mathrm{Tukey}}$ refers to the tapering parameter of the Tukey window, denoting the fractional length of the window's central unitary plateau. $T_{\mathrm{obs}}$ is the observing time of the run. $t_{\mathrm{mid}}$ represents the mean time between the start and the end of the run measured in GPS seconds. $\Delta f$ refers to the bandwidth of the individual subbands analyzed by each computing job.

| Search setup parameter | Value |
|---|---|
| $T_{\mathrm{SFT}}$ | 1024 s |
| $\beta_{\mathrm{Tukey}}$ | 0.5 |
| $T_{\mathrm{obs}}$ | 14832675 s |
| $t_{\mathrm{mid}}$ | 1245582821.5 s |
| $\Delta f$ | 0.125 Hz |

TABLE II. Number of short Fourier transforms (SFTs) in each of the datasets. Characteristics of these SFTs are summarized in Table I and Sec. III.

| | Nonoverlapping | Overlapping |
|---|---|---|
| H1 | 10172 | 20577 |
| L1 | 10962 | 22049 |
| Total | 21234 | 42626 |

## IV. THE SEARCH PIPELINE

We split the search into two main frequency bands: the low-frequency band, from 50 Hz to 100 Hz, and the high-frequency band, from 100 Hz to 300 Hz. These bands are further divided into $\Delta f = 0.125$ Hz subbands, which constitute the basic working unit of our setup: each *computing job* performs an all-sky search over one such subband, searching for binary modulated signals within a certain region of the binary parameter space among the ones specified in Fig. 1 and Table III. Because of the limited computing power available, the high-frequency search focuses on a single binary parameter space region, denoted as B in Table III; the low-frequency search is performed in all four binary parameter space regions.

The search parameter space is gridded with templates as described in [13]

$$\delta f_0 = \frac{1}{T_{\mathrm{SFT}}}, \qquad \delta\theta = \frac{c/v}{T_{\mathrm{SFT}} f_0 P_{\mathrm{f}}}, \qquad \delta a_p = \frac{\sqrt{6m}}{\pi T_{\mathrm{SFT}} f_0 \Omega},$$

$$\delta\Omega = \frac{\sqrt{72m}}{\pi T_{\mathrm{SFT}} f_0 a_p \Omega T_{\mathrm{obs}}}, \qquad \delta t_{\mathrm{asc}} = \frac{\sqrt{6m}}{\pi T_{\mathrm{SFT}} f_0 a_p \Omega^2}, \qquad (7)$$

where $\delta\theta$ refers to the angular sky position resolution, $v = |\vec{v}|$, and $v/c \sim 10^{-4}$. $T_{\mathrm{obs}}$ denotes the observing time of the search, quoted in Table I. The variables $P_{\mathrm{f}}$ and $m$ are the so-called *pixel factor* and *mismatch* parameters, which can be used to manually control the parameter space template
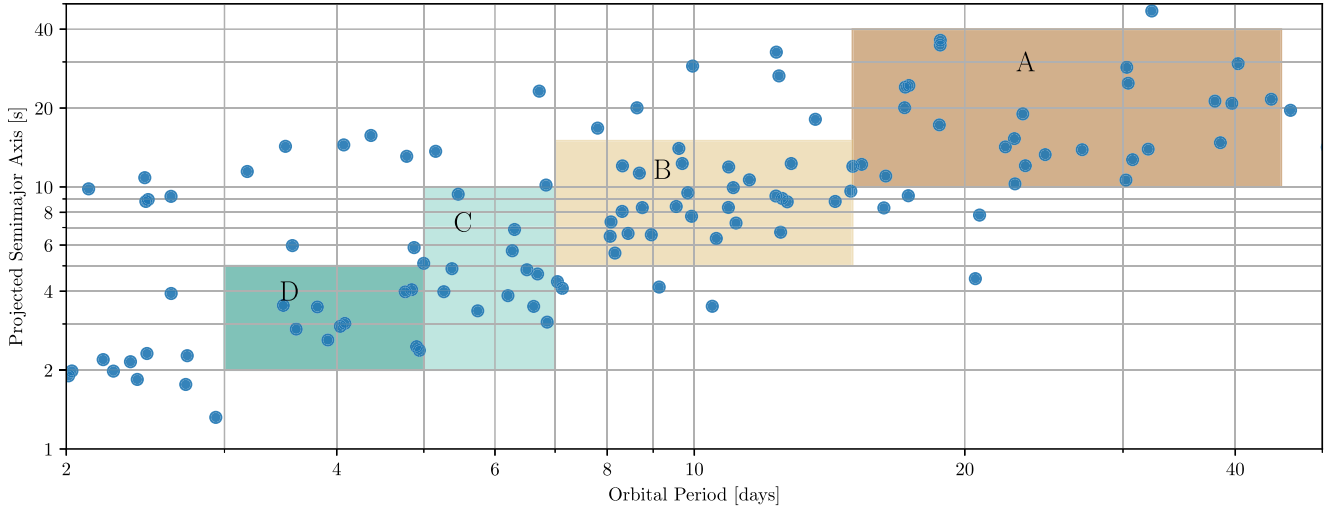
FIG. 1. Binary orbital parameters considered by the present search. Solid color regions denote parameter space regions in which a search was performed; blue dots mark binary orbital parameters corresponding to the known binary pulsar population. Regions A, B, C, and D were covered by the low-frequency analysis, while region B was covered by the high-frequency analysis as well. Time of ascending node passage is taken into account according to the orbital frequency, as explained in Sec. II. Pulsar population data was taken from [14] using [24].

density. In this search, we tune them in order to adjust the computing cost as we reach higher frequencies, where template spacing naturally becomes finer. Table IV summarizes the choices made for each of the frequency bands.

The pipeline uses the Hough transform to relate tracks in the digitized spectrogram, as explained below, to points in the parameter space. For each point in the parameter space $\lambda \in \mathbb{P}$, there is a corresponding track [see Eq. (6)] of the time-frequency evolution, which denotes the instantaneous frequency of the signal as observed by the detector.

### A. Ranking statistics

Let us assume the data can be described as a noise background plus a CW signal,

$$x(t; \lambda) = n(t) + h(t; \lambda). \tag{8}$$

We start by computing the *normalized power* of SFT data,

$$\rho_k^\alpha = \frac{|\tilde{x}_k^\alpha|^2}{\langle |\tilde{n}_k^\alpha|^2 \rangle}, \tag{9}$$

TABLE III. Binary parameter space regions analyzed by the search, corresponding to the four colored regions in Fig. 1. Time of passage through the ascending node $t_{\text{asc}}$ is searched along the interval specified in Sec. II.

| Binary region | $P$ [days] | $a_p$ [s] |
|---|---|---|
| A | [15, 45] | [10, 40] |
| B | [7, 15] | [5, 15] |
| C | [5, 7] | [2, 10] |
| D | [3, 5] | [2, 5] |

where tildes represents a Fourier transformed quantity, $k$ indexes frequency bins, $\alpha$ indexes SFTs, and $\langle \cdot \rangle$ denotes a running median average using 101 frequency bins, as explained in [13]. Each SFT $\alpha$ can be related to a certain starting time $t_\alpha$, effectively obtaining a spectrogram where each bin $(\alpha, k)$ corresponds to the normalized power $\rho_k^\alpha$ present at a certain frequency bin $k$ in a certain SFT $\alpha$. Then, we impose a normalized power threshold $\rho_{\text{th}} = 1.6$ to digitize the spectrogram, obtaining a discrete spectrogram populated by ones and zeros.

For each template, we follow the corresponding track and define the first ranking statistic, the *number count*, as the weighted sum of ones and zeroes,

$$n(\lambda) = \sum_{(\alpha, k) \in f_\lambda} w_k^\alpha \mathcal{H}(\rho_k^\alpha - \rho_{\text{th}}), \tag{10}$$

where $\mathcal{H}$ denotes the Heaviside step function, and the weights $w_k^\alpha$ account for varying noise floor and antenna response effects [25].

TABLE IV. Mismatch and pixel factor configurations for the different frequency bands of the search. L refers to the low-frequency band; H1-5 refer to each of the five subbands into which the high-frequency band was partitioned: 1 and 2 span 25 Hz each, while 3 to 5 span 50 Hz each.

| Label | Frequency [Hz] | $m$ | $P_f$ |
|---|---|---|---|
| L | [50, 100) | 0.4 | 1 |
| H1 | [100, 125) | 0.4 | 1 |
| H2 | [125, 150) | 0.6 | 1 |
| H3 | [150, 200) | 0.9 | 0.8 |
| H4 | [200, 250) | 1.6 | 0.75 |
| H5 | [250, 300) | 2 | 0.7 |

The number count statistic can be efficiently computed by means of the look up table (LUT) approach described in [15]. Incidentally, this strategy simplifies the cost by analyzing multiple sky positions (called *sky patches*) together. The approach applies the Doppler modulation used to analyze a particular frequency bin to a neighborhood of frequency bins. The sensitivity loss introduced by this approximation is later compensated by reanalyzing the most significant candidates using their exact time-frequency tracks [26].

The reanalysis uses the *weighted normalized power* statistic,

$$\rho(\lambda) = \sum_{(\alpha,k)\in f_\lambda} w_k^\alpha \rho_k^\alpha. \tag{11}$$

Using this new ranking statistic instead of simply recomputing Eq. (10) along the exact track yields a 10–20% improvement in detection efficiency for the top lists (ranking of the most significant candidates) based on the number-count statistic used here and discussed below [8].

In order to further select candidates across different sky patches, we compute a *significance* statistic by normalizing Eq. (11) to the *expected noise values* derived in [15]

$$s_\rho(\lambda) = \frac{\rho(\lambda) - \bar{\rho}}{\sigma_{\bar{\rho}}}, \tag{12}$$

where $\bar{\rho}$ and $\sigma_{\bar{\rho}}$ represent the expected value and standard deviation of weighted normalized power in pure Gaussian noise. This statistic removes any dependency on the sky position of the source due to the weights, being well suited for comparisons across different sky patches.

### B. Top list construction

Top lists are constructed frequency-bin-wise across sky patches, as shown schematically in Fig. 2. For a given sky patch and frequency bin, the top 5% of parameter space candidates are selected according to the number count

---

**Result:** Toplist per 0.125 Hz sub-band
Select 0.125 Hz sub-band;
**for** *SkyPatchIndex p* **do**
    Initialize per-patch toplist *p*;
    **for** *FrequencyBinIndex k* **do**
        Rank candidates by number count (10);
        Select top 5 candidates;
        Rank candidates by norm. power (11);
        Select top 0.1 candidates;
        Write candidates into per-patch toplist *p*;
    **end**
**end**
Initialize sub-band toplist;
Collect all per-patch toplists into sub-band toplist;
Rank sub-band toplist by significance (12);
Select top 80000 candidates.

FIG. 2. Explicit description of the BINARYSKYHOUGH toplist construction process.

---

statistic Eq. (10), using the LUT approach and the non-overlapping set of SFTs. Then, they are reanalyzed computing their corresponding normalized power Eq. (11) along the exact time-frequency evolution given by Eq. (6) using the overlapping set of SFTs. Finally, top candidates according to Eq. (12) are collected into a final top list. We collect the top 80000 candidates from each 0.125 Hz subband.

This approach optimizes the GPU usage in the number count stage (preventing loud spectral artifacts from saturating the top list) as each frequency bin provides a controlled number of candidates.

## V. POST PROCESSING

Similar to previous searches [8,16], we apply a clustering algorithm to the resulting candidates in order to look for particularly interesting candidates. Clustering candidates reduces the total number of candidates to follow up since, typically, many candidates are found to be produced by a single source (either a CW signal or an instance of instrumental noise).

We implement a new clustering algorithm using the frequency evolution of a candidate to define a parameter space distance [27]. This choice allows the algorithm to naturally take into account the parameter space structure, avoiding the usage of *ad hoc* sky projections or mishandling periodic boundary conditions.

After the cluster selection, we apply the well-known *line veto*, used in previous searches (e.g., [8,16,28,29]) in order to rule out non-astrophysical candidates.

### A. Clustering

The clustering algorithm is summarized below; see [27] for further details. Given two candidates with template values $\lambda, \lambda^* \in \mathbb{P}$, we define the parameter space distance as

$$d(\lambda^*, \lambda) = \frac{T_{\text{SFT}}}{N_\alpha} \sum_{t_\alpha} |f_{\lambda^*}(t_\alpha) - f_\lambda(t_\alpha)|, \tag{13}$$

where $f_\lambda(t_\alpha)$ represents the instantaneous frequency of a CW produced by a source with parameters $\lambda$ as measured by the detector at time $t_\alpha$, and $N_\alpha$ denotes the number of SFT timestamps used. Essentially, Eq. (13) is the average mismatch among time-frequency tracks.

Clusters are formed by grouping together candidates from connected components; *i.e.*, each candidate in a cluster is closer than a maximum distance $d^{\text{th}} = 1$ to at least one other candidate in the same cluster. Final clusters are ranked according to the significance of their loudest candidate, which we will refer to as the *cluster center*.

For each 0.125 Hz top list, the top five clusters according to their significance are selected. This leaves us with a total of 16000 clusters: 8000 for the high-frequency search and 2000 for each region of the low-frequency search.

TABLE V. Numbers of cluster centers discarded by the line veto using lines present in [30]. The number of surviving outliers after the follow-up stage (see Sec. VII) is here specified for the sake of completeness. Five clusters were collected from each 0.125 Hz band; regions H1B and H2B, being the only ones spanning 25 Hz, yield a lower number of clusters.

| Regions | LA | LB | LC | LD | H1B | H2B | H3B | H4B | H5B |
|---|---|---|---|---|---|---|---|---|---|
| Initial clusters | 2000 | 2000 | 2000 | 2000 | 1000 | 1000 | 2000 | 2000 | 2000 |
| Vetoed by identified line | 366 | 359 | 359 | 373 | 44 | 0 | 32 | 30 | 30 |
| Surviving clusters | 1634 | 1641 | 1641 | 1627 | 956 | 1000 | 1968 | 1970 | 1970 |
| Fraction (%) | 81.7 | 82.05 | 82.05 | 81.35 | 95.6 | 100 | 98.4 | 98.5 | 98.5 |
| Surviving outliers after $2\hat{\mathcal{F}}_{\text{th}}$ veto | 73 | 72 | 71 | 71 | 7 | 6 | 8 | 3 | 0 |

## B. Line veto

Before the outlier follow-up, we apply the line veto to the obtained cluster centers. Using the list of identified narrow spectral artifacts [30], the veto discards any candidate whose time-frequency track crosses an instrumental line, since such a candidate would likely become significant not because of astrophysical reasons but rather instrumental ones.

For every cluster center with parameters $\lambda$, we compute its *bandwidth*,

$$\mathcal{BW}(\lambda) = [\min_{t_\alpha} f_\lambda(t_\alpha), \max_{t_\alpha} f_\lambda(t_\alpha)]. \quad (14)$$

If the bandwidth of a candidate contains or overlaps with any of the lines present in [30], then the candidate is discarded because of its likely nonastrophysical origin. This veto reduces the number of clustered candidates by ~20% in the low-frequency search and by a few percent in the high-frequency search (see Table V). This difference is to be expected, considering the greater amount of instrumental lines present at lower frequencies.

Other narrow spectral artifacts have not yet been identified as clearly nonastrophysical in origin in an unidentified list [31]. Although this list has not been used to veto clustered candidates, some of them are consistent with artifacts in the unidentified list (see Appendix).

## VI. SENSITIVITY

The sensitivity of the search is determined using a similar procedure as for previous all-sky searches [8,16,28,29]. A campaign of adding software-simulated signals to the data in order to estimate the $h_0$ that corresponds to a 95% average detection rate was carried out. We quantify sensitivity using the *sensitivity depth* [32,33],

$$\mathcal{D} = \frac{\sqrt{S_n}}{h_0}, \quad (15)$$

where $S_n$ represents the single-sided power spectral density of the data (PSD), $\sqrt{S_n}$ is referred to as the amplitude spectral density (ASD), and $h_0$ is the previously defined CW amplitude. This figure of merit characterizes the

sensitivity of the search to putative signals and accounts for the detector sensitivity as a function of frequency. The actual single-sided PSD in Eq. (15) depends on the analysis method being used. BinarySkyHough sensitivity is dominated by the first stage using the weighted number count statistic, meaning one should use the *inverse squared averaged* PSD as shown in Eqs. (42) to (44) of [34],

$$S_n(f) = \sqrt{\frac{N_\alpha}{\sum_\alpha [S_\alpha(f)]^{-2}}}, \quad (16)$$

where $S_\alpha(f)$ represents the running-median noise floor estimation using 101 bins corresponding to the SFT labeled by starting time $t_\alpha$ at frequency $f$. The goal is to characterize the average detection rate by numerically computing the efficiency distribution with respect to the depth. The result is interpolated to find the estimated sensitivity depth that corresponds to 95% detection efficiency. Using Eq. (15), the sensitivity depth is converted to the sensitivity amplitude. It is in this last step where the systematic error of the calibration is potentially relevant.

Systematic error in the amplitude of calibration of C01 data (final calibration version) is estimated to be lower than 7% (68% confidence interval) for both detectors over all frequencies throughout O3a [20]. Relative deviations of ASDs computed using C00 data with respect to ASDs computed using C01 data (used as a proxy for an estimate of systematic error in C00 data calibration, which, otherwise, does not exist for all time or frequencies) are below 7% for all frequency bands except in the [59,61] Hz subband, where the relative deviation is 10%. Assuming the proxy for C00 systematic error is complete, the impact of such 10% level of systematic error is negligible to the conclusions of this analysis.

Five representative frequency bands are selected across each 25 Hz band and binary parameter space region and five sensitivity depth values used, namely [18, 20, 22, 24, 26] Hz$^{-1/2}$. Two hundred signals drawn from uniform distributions in phase and amplitude parameters are added to the data at each depth, band, and binary parameter space region. For each simulated signal, BinarySkyHough analyzes the data again in order to evaluate how many of them are detected. Sensitivity depth values are selected such that the

95% efficiency depth was properly bracketed; regions H4B and H5B required two extra depth values $[14, 16]$ Hz$^{-1/2}$ to ensure this. Using a small number of frequency bands drastically reduces the computing cost of the sensitivity estimation procedure while yielding consistent results when compared to an exhaustive injection campaign, as justified in [16].

Three criteria must be fulfilled in order to label a simulated signal as "detected." First, the top list obtained from the injection search should contain at least one candidate whose significance Eq. (12) is greater than the minimum significance present in the corresponding all-sky top list. Second, after clustering the injection top list, at least one cluster with a significance greater than the lowest significance recovered by the corresponding all-sky clustering must be obtained. These two criteria ensure the injection is prominent enough so as not to be discarded by the first stage of the search. Lastly, we require at least one of the top five clusters from the injection top list to be located closer than two parameter space bins in each of the parameters with respect to the injection parameters. This last criterion takes into account the fact that, in the actual search, a follow-up will be done in corresponding regions around each significant cluster center.

After separating detected from nondetected simulated signals, we construct efficiency curves akin to the example shown in Fig. 3. Each point is the fraction of simulated signals detected (*i.e.*, detection efficiency) as a function of the sensitivity depth. For each sensitivity depth set of $N_I = 200$ simulated signals, the uncertainty on detection efficiency $E$ is given by

$$\delta E = \sqrt{\frac{E \cdot (1 - E)}{N_I}}. \qquad (17)$$

Then, using SciPy's `curve_fit` function [35], we fit a sigmoid curve to the data given by

$$S(\mathcal{D}; \vec{p}) = 1 - \frac{1}{1 + e^{-p_0(\mathcal{D} - p_1)}}, \qquad (18)$$

with fitted parameters $\vec{p} = (p_0, p_1)$. This expression can be inverted in order to find the 95% sensitivity depth.

The interpolations are accompanied by a corresponding uncertainty, obtained through the covariance matrix of the fit $\mathcal{C}(\mathcal{D})$ as

$$\delta \mathcal{D}^{95\%} = \sqrt{\vec{p}^{\mathrm{T}} \cdot \mathcal{C}(\mathcal{D}) \cdot \vec{p}}\Big|_{\mathcal{D} = \mathcal{D}^{95\%}}. \qquad (19)$$

The resulting interpolated depths per frequency band are shown in Fig. 4. The high-frequency search shows a clear degradation of depth values as frequency increases. This is related to the decaying density of parameter space templates: The higher the frequency, the finer one must
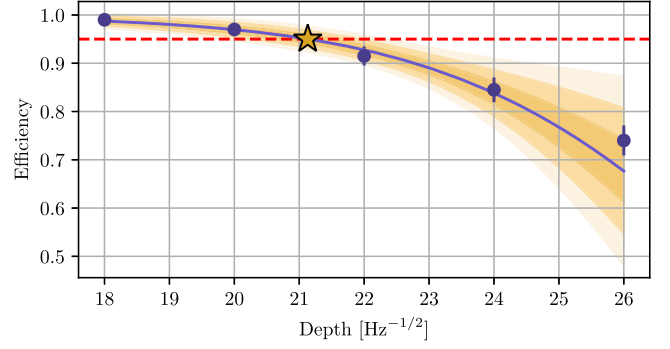


FIG. 3. Example of 95% sensitivity depth interpolation. Five sensitivity depths were selected at 124.625 Hz in region H1B, and 200 injections were injected at each of these depths, applying the criteria exposed in the text in order to label injections as detected or not detected. Blue dots represent the fraction of detected injections; the sigmoid fit is represented by a blue line; fit uncertainties at one, two, and three sigmas are represented by pale yellow shades. The interpolated 95% sensitivity depth $\mathcal{D}^{95\%} = 21 \pm 0.4$ is marked using a star.
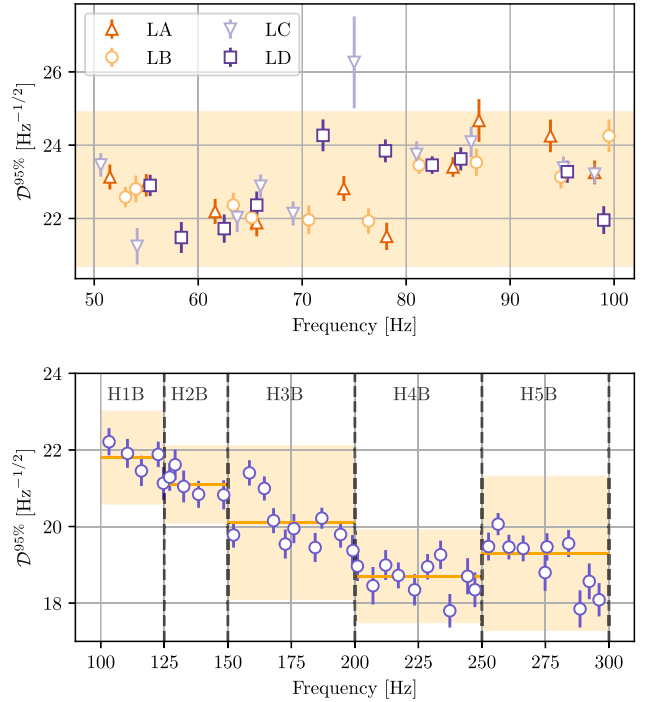


FIG. 4. Average 95% sensitivity depths obtained in the low-frequency (top panel) and high-frequency (bottom panel) bands. Data points correspond to the interpolated results obtained through the sigmoid fit of the efficiencies at the selected frequency bands (five bands randomly selected in each 25 Hz). Error bars correspond to 95% efficiency uncertainties toward low depth values. Shaded regions show the averaged results with their uncertainties, as summarized in Table VI. In the top panel, shading is only shown for the results obtained for the binary parameter space region B.

TABLE VI.   Average 95% sensitivity depths for the parameter space regions analyzed in this search. Region labels are defined in Tables III and IV.

| Region | $\langle \mathcal{D}^{95\%} \rangle \pm 3\sigma [\mathrm{Hz}^{-1/2}]$ |
|--------|-----------------------------------------------------------|
| LA | $22.9 \pm 2.5$ |
| LB | $22.8 \pm 2.1$ |
| LC | $23.0 \pm 2.5$ |
| LD | $23.0 \pm 2.5$ |
| H1B | $21.8 \pm 1.2$ |
| H2B | $21.1 \pm 1.0$ |
| H3B | $20.1 \pm 2.0$ |
| H4B | $18.7 \pm 1.2$ |
| H5B | $19.3 \pm 2.0$ |

construct a template bank in order to achieve a comparable level of sensitivity.

Finally, we compute an average 95% sensitivity depth for each of the regions quoted in Table VI. We also quote a corresponding $3\sigma$ uncertainty, which previous studies have proven to deliver a good coverage of the actual 95% efficiency sensitivity depth [16]. These values are translated to CW amplitude $h_0$ via Eq. (15) and shown in Fig. 5.

## VII. FOLLOW-UP

Remaining candidates from the main search are followed up applying a more sensitive method to the data. Longer coherence times constrain the phase evolution of the candidate under consideration and would yield higher significance for a true continuous wave signal. A potential downside remains that a true signal could be discarded if it is not well modeled by the assumed phase evolution. Moreover, increasing the coherence time also requires

increasing the density of templates so as not to overlook a putative signal.

An effective way to cover small parameter regions is through Markov Chain Monte Carlo (MCMC) methods, which, rather than following a prescribed parameter space grid, sample the parameter space following a certain probability density function. Reference [36] describes how this can be implemented in a search for continuous waves by using the so-called $\mathcal{F}$ statistic, a well-established CW analysis technique, as a likelihood function. We refer to [36] and references therein for an in-depth explanation of this method.

The $\mathcal{F}$ statistic is a coherent statistic, usually referred to as $2\tilde{\mathcal{F}}$, which compares data against templates by matched filtering. A semicoherent $\mathcal{F}$-statistic $2\hat{\mathcal{F}}$ can be defined by adding individual $2\tilde{\mathcal{F}}$ values computed over $N_{\mathrm{seg}}$ segments spanning $T_{\mathrm{coh}}$ each, in the same way as weighted normalized power was computed from weighted power in Eq. (11):

$$2\hat{\mathcal{F}}(\lambda) = \sum_{s=0}^{N_{\mathrm{seg}}-1} 2\tilde{\mathcal{F}}_s(\lambda), \qquad (20)$$

where the index $s$ indicates the coherent quantity has been computed for a certain segment spanning $T_{\mathrm{coh}}$.

We use software injections in order to calibrate a threshold $2\hat{\mathcal{F}}_{\mathrm{th}}$. Candidates such that $2\hat{\mathcal{F}}(\lambda) < 2\hat{\mathcal{F}}_{\mathrm{th}}$ will be deemed as nonsignificant and consequently discarded.

This algorithm is implemented in PyFstat [37,38]. It builds on top of LALSuite [39], which provides the CW data analysis functionality, and PTEMCEE [40,41], which implements the MCMC algorithms.
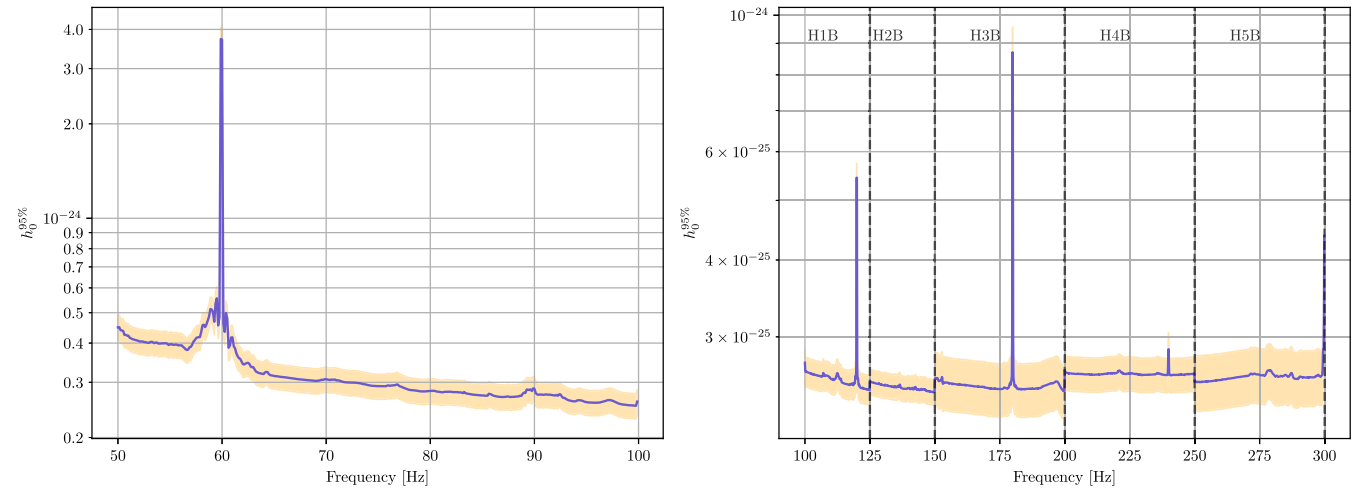


FIG. 5.    Implied 95% efficiency amplitude from the obtained sensitivity depth values. The $h_0^{95\%}$ amplitude estimates are obtained from the 95% efficiency depth values shown in Table VI and the *inverse squared averaged* PSD using Eq. (15). Low-frequency results are shown for binary parameter space region B.

## A. MCMC follow-up configuration

The MCMC follow-up employed is not intended to describe the posterior distribution of parameters defining a candidate. Rather, we only require enough convergence such that the sampled $\mathcal{F}$-statistic values are close enough to the local maximum to establish a reliable veto threshold.

### 1. Sampler configuration

The PTEMCEE package implements an ensemble-based sampler that uses several walker chains to sample multimodal distributions. Expensive setups are not required in order to perform a first-stage follow-up using a threshold-based approach. The reason for this is twofold: We are increasing the coherence time with respect to the search, and we do not require extensive convergence to be achieved. No second-stage follow-up was required because all of the first-stage outliers were attributed to instrumental causes. If this was not the case, we would have applied a second follow-up stage using a more expensive setup. The number of parallel chains, walkers per chain, and number of steps to take are summarized in Table VII.

We choose to use $N_{\text{seg}} = 260$, which corresponds to $T_{\text{coh}} \simeq 17$ h. This is a longer coherence time with respect to that of the initial stage of the search, a choice used in previous searches [16].

### 2. Prior choice

Following a similar prescription as the one given in [36], we set up uniform priors in each parameter space dimension, forming a box centered on each cluster center. Each edge of this box spans two parameter space bins according to the spacing given in Eq. (7), where the parameter-space-dependent quantities are computed at the center of the cluster. This is in agreement with the detection criteria imposed to perform the sensitivity estimation.

Although BinarySkyHough targets CW sources in circular orbits, it is still sensitive to signals with eccentricities up to a certain value, as long as the Doppler modulation derived from eccentricity is smaller than half a frequency bin. The upper bound for the maximum allowable eccentricity according to this argument was derived in [13]

$$e^{\text{m.a.}} = [2T_{\text{SFT}}f_0 a_p \Omega]^{-1}. \tag{21}$$

TABLE VII. MCMC hyperparameter choice for the first stage of the follow up. Each of the *parallel chains* samples the likelihood at a different temperature, as explained in [41].

| Hyperparameter | Value |
| --- | --- |
| Parallel chains | 3 |
| Walkers per chain | 100 |
| Burn-in production steps | $100 + 100$ |

Therefore, uniform priors on eccentricity, $[0, e^{\text{m.a.}}]$, and argument of periastron, $[0, 2\pi]$, are included as MCMC parameters. Maximum eccentricities range from 0.2–0.5 at 50 Hz to less than 0.1 at 300 Hz.

## B. Setting up a threshold

We use the BinarySkyHough and the MCMC follow-up on a total of 71306 software injections in order to calibrate a significance threshold. The employed injections are consistent with the ones used for the sensitivity estimation, focusing on those detected according to the three criteria (see Sec. VI). This implies a significant fraction of the injections will possess an amplitude below the obtained 95% sensitivity amplitude, as they will be distributed according to the five original depths. The threshold obtained using this calibration strategy will have a low false-dismissal rate ($\lesssim 1/71306 \simeq 1.5 \times 10^{-5}$) against signals detectable by this pipeline.

We run the MCMC algorithm in order to sample $2\hat{\mathcal{F}}$ values, retrieving the maximum value for each of the injections. Resulting $2\hat{\mathcal{F}}$ values for these simulations are plotted in Fig. 6. These results support the choice of
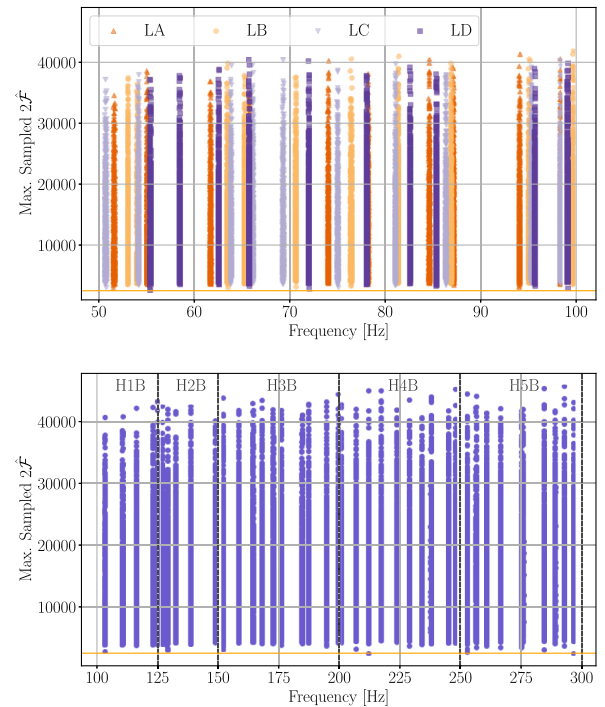


FIG. 6. Recovered $2\hat{\mathcal{F}}$ values using a set of injections labeled as *detected* by the sensitivity estimation criteria. The amplitudes of these injections were distributed using the five sensitivity depth values explained in Sec. VI. The top panel shows the results for the four regions of the low-frequency search, involving 33757 injections; the bottom panel shows the same result for the high-frequency search, using 37549 injections. The horizontal orange line marks the threshold $2\hat{\mathcal{F}}_{\text{th}} = 2500$.

$2\hat{\mathcal{F}}_{\text{th}} = 2500$ as the threshold value, with all detected injections above this threshold.

## C. Surviving outliers

After executing the MCMC follow-up and imposing the $2\hat{\mathcal{F}}_{\text{th}} = 2500$ threshold, 287 outliers remain in the low-frequency band, and 24 outliers remain in the high-frequency band, as shown in Fig. 7. It is clear from the figure that low-frequency outliers mostly belong to the same frequency bands across the four binary parameter space regions. We next analyze each candidate using a cumulative semicoherent $\mathcal{F}$ statistic, defined as

$$2\hat{\mathcal{F}}(\lambda; t) = \sum_{\alpha: t_\alpha < t} 2\tilde{\mathcal{F}}_\alpha(\lambda), \qquad (22)$$

in order to discern those candidates originating from instrumental noise.

We use three flavors of Eq. (22), one for each of the detectors (H1 and L1) and another one using a multi-detector approach (H1 + L1). These statistics lead to the rejection of the remaining outliers, as described below.

### 1. Line-crossing outliers

CWs are expected to accumulate a $2\hat{\mathcal{F}}$ value linearly with respect to the observing time. We find that 263 outliers surpass the $2\hat{\mathcal{F}}_{\text{th}} = 2500$ threshold due to the presence of prominent values of segment-wise $\mathcal{F}$ statistic at certain times of the run in one of the detectors (260 in H1 and 3 in L1), as exemplified in Fig. 8. The higher number of outliers in H1 arises from the greater number of instrumental lines present in that detector [30,31].

This behavior would be expected from a candidate whose frequency evolution track crosses a narrow instrumental artifact (line) for a limited duration, either because of the frequency track drifting away from the line or the transient nature of the line itself. Most strong persistent instrumental disturbances are already discarded using the known lines list [30], but weaker lines or transient disturbances (lasting hours to days), which are more difficult to identify in the run-averaged spectra, could still affect our searches [21,42].

In Table VIII in Appendix, we present a list of frequency bands containing these 263 candidates whose behavior suggests a brief line crossing or the presence of a transient instrumental disturbance. Outliers were selected as belonging to this category if they have at least one per-segment $\mathcal{F}$-statistic value greater than 100, and for each frequency band listed in the table, the first and last timestamps bracket the data segments where $\mathcal{F}$-statistic values greater than 50 were observed for at least one of those candidates. Overlapping frequency bands were merged together for the sake of clarity.
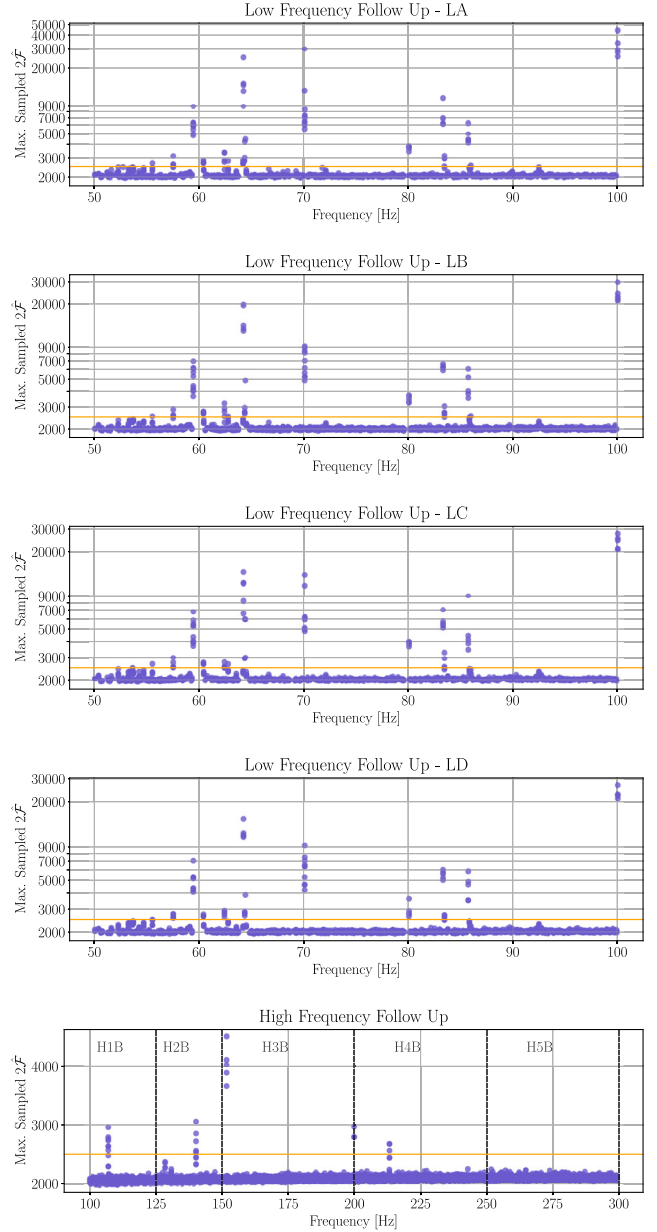


FIG. 7. MCMC follow-up results. Dots represent cluster centers not vetoed by the identified line veto, and a horizontal line represents the imposed threshold $2\hat{\mathcal{F}}_{\text{th}} = 2500$, calibrated by software injections (see Fig. 6). The horizontal axis represents the frequency value associated to each cluster center, and the vertical axis represents the maximum $2\hat{\mathcal{F}}$ value sampled by the MCMC run.

### 2. Detector consistency veto

A second set of 28 outliers is discarded by the detector consistency veto (see e.g., [28]). During O3a, the L1 detector presents a better sensitivity than H1 at low frequencies [19]. A CW candidate would be expected to behave consistently; *i.e.*, $2\hat{\mathcal{F}}_{\text{L1}} > 2\hat{\mathcal{F}}_{\text{H1}}$ for most signals. We calibrate this veto using the aforementioned set of software injections in order to take detector sensitivity
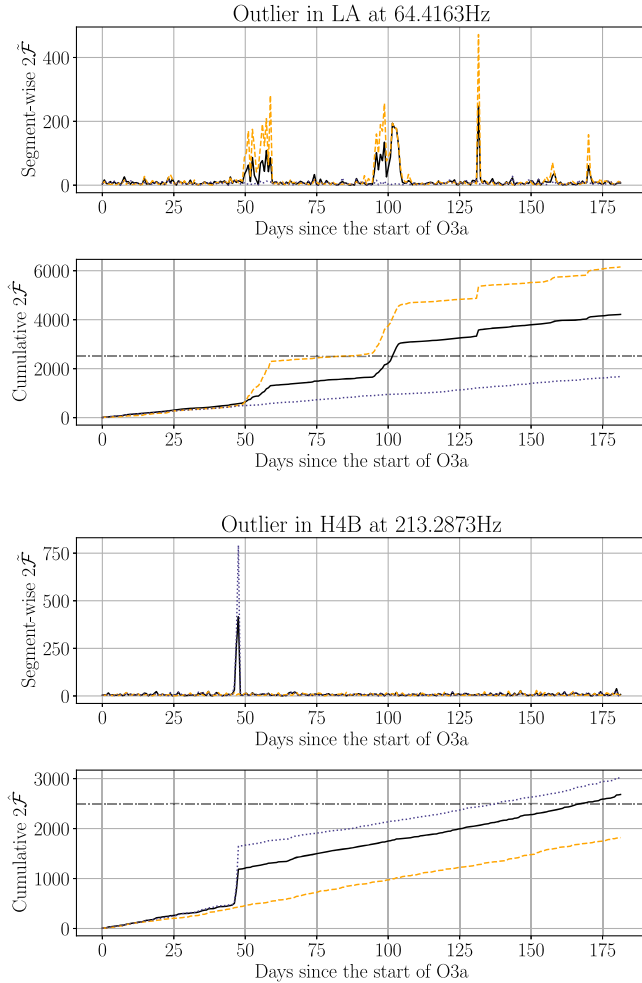
FIG. 8. Example of outliers produced by instrumental noise in one of the Advanced LIGO detectors. Each pair of panels corresponds to a different outlier; the segment-wise $2\tilde{\mathcal{F}}_\alpha$ statistic is shown at the top of each pair; the cumulative semicoherent $2\hat{\mathcal{F}}$ as described in Eq. (22) is shown at the bottom of each pair. Dashed lines denote an H1-only analysis, dotted blue lines an L1-only analysis, and solid black lines a multidetector analysis. The $2\hat{\mathcal{F}}_{\rm th} = 2500$ threshold is shown as a horizontal line.

anisotropies due to the antenna pattern functions into account, obtaining a maximum relative 5% excess of $2\hat{\mathcal{F}}_{\rm H1}$ with respect to $2\hat{\mathcal{F}}_{\rm L1}$.
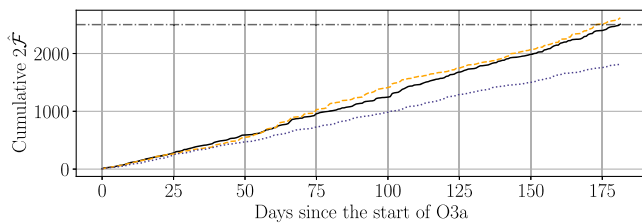


FIG. 9. Example of an outlier vetoed by the multidetector consistency veto. Dashed lines denote an H1-only analysis, dotted blue lines an L1-only analysis, and solid black lines a multi-detector analysis. The $2\hat{\mathcal{F}}_{\rm th} = 2500$ threshold is shown as a horizontal line.
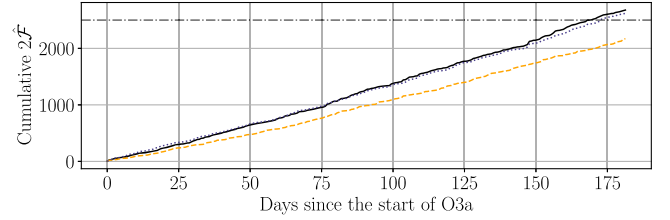


FIG. 10. Example of an outlier surpassing the $2\hat{\mathcal{F}}_{\rm th} = 2500$ threshold later vetoed by inspection of the detector spectra. The combined ASD of both detectors around the frequency of this group of outliers is shown in Fig. 11. Candidates related to this signal saturated the top list in the four regions LA, LB, LC, LD. Dashed lines denote an H1-only analysis, dotted blue lines an L1-only analysis, and solid black lines a multidetector analysis. The $2\hat{\mathcal{F}}_{\rm th} = 2500$ threshold is shown as a horizontal line.

The 28 outliers rejected with this veto show more than a 30% relative excess of $2\hat{\mathcal{F}}_{\rm H1}$ with respect to $2\hat{\mathcal{F}}_{\rm L1}$. Hence, we discard them as being inconsistent with an astrophysical signal. Figure 9 shows an example of these outliers. After computing the bandwidth covered by each of these candidates, we obtain seven distinct frequency bands affected by instrumental disturbances of this type, summarized in Table IX in appendix.

### 3. Powerline sidebands

The last 20 outliers were consistently present in each one of the four parameter space regions within the [60.46,60.48] Hz subband. These outliers were not vetoed by any of the previous stages. As shown in Fig. 10, $2\hat{\mathcal{F}}$ was accumulated in a fairly linear fashion, achieving greater values in L1 than H1. The detector ASD (Fig. 11), however, shows that these candidates were caused by sidebands of the 60 Hz power supply artifact. These sidebands can be explained by a nonlinear coupling between the main power supply frequency and a low-frequency noise. They do not appear in the line lists [30,31] as they do not correspond to
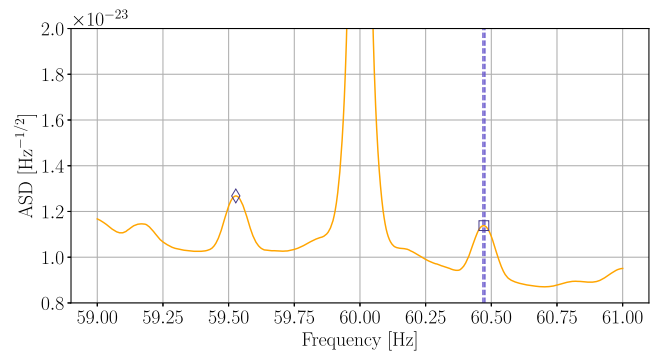


FIG. 11. Location of the manually inspected outliers (vertical dashed line) with respect to the amplitude spectral density of the detector, here represented as a multidetector *inverse squared average* (orange line). A diamond and a square mark the twin peaks' frequency, 59.53 Hz and 60.47 Hz, respectively.
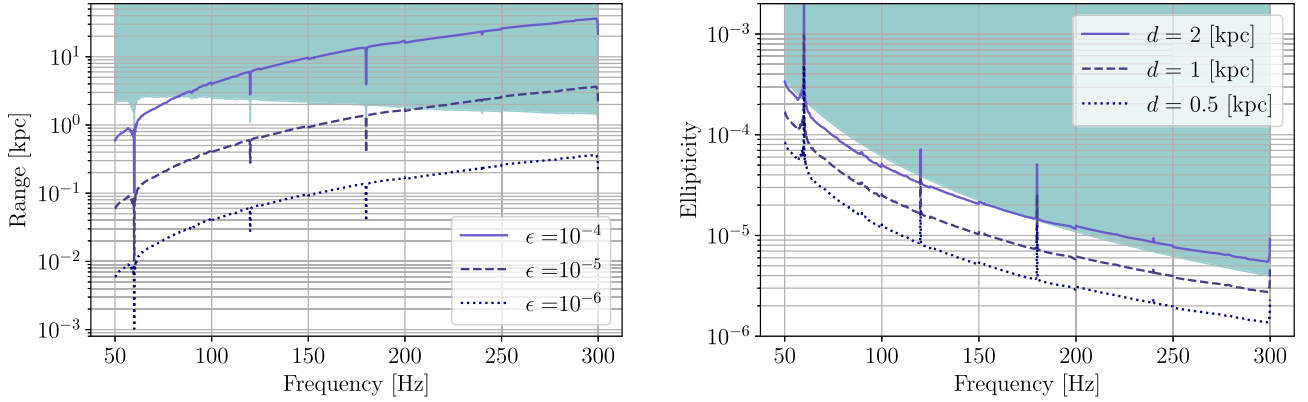
FIG. 12.   Astrophysical reach (left) and equatorial ellipticity (right) implied by the search sensitivity $h_0^{95\%}$. These results were obtained assuming a canonical neutron star moment of inertia $I_z = 10^{38}$ kg $\cdot$ m$^2$. Shaded areas denote regions excluded due to the spin-down limit implied by the maximum spin-down value considered in this search.

narrow spectral artifacts, and their effect on CW searches is highly dependent on the search method. Due to the presence of said artifact in the data and the wide spread of the candidates obtained by our search across these bands, we deem this final set of candidates as nonastrophysical.

## VIII. CONCLUSION

We report on a search for continuous gravitational wave signals from unknown sources in binary systems using LIGO data from the first six months of the third Advanced LIGO and Advanced Virgo observing run. Four different binary parameter space regions, spanning orbital periods of three to 45 days and projected semimajor axes of two to 40 light seconds, are searched across the 50–300 Hz frequency band. We claim no detections and estimate the sensitivity of the search in terms of the gravitational wave amplitude corresponding to the interpolated 95% detection efficiency using a simulated population of signals.

The minimum amplitude sensitivity attains an average value of $h_0^{95\%} = (2.4 \pm 0.1) \times 10^{-25}$ in the $f_0 = 149.5$ Hz subband. This is a factor of ~1.6 lower than the lowest amplitude sensitivity obtained by a previous search performed on data from the second Advanced LIGO observing run [16]. The estimated amplitude sensitivity can be interpreted in terms of astrophysical reach and equatorial ellipticity by means of equation Eq. (2), as shown in Fig. 12.

The validity of this estimation must be discussed in terms of the *spin-down limit*, which corresponds to the maximum gravitational wave amplitude achievable by a neutron star assuming its rotational energy is solely lost via gravitational waves. We refer the reader to Appendix A of [6] for its definition and the relevant conversion equations.

The maximum spin-down value probed by our search is $|\dot{f}_0| \equiv (T_{\text{SFT}} \cdot T_{\text{obs}})^{-1} \simeq 6.5 \times 10^{-11}$ Hz/s [13], meaning sources braking at higher rates would not be detected by our pipeline (see Table I for the definition of $T_{\text{SFT}}$ and $T_{\text{obs}}$). Assuming the canonical emission model of a deformed NS

as in Eq. (2), this implies the existence of a distance beyond which the required ellipticity to emit a detectable amplitude would imply a greater spin-down than the one probed by the search, as long as no processes balancing the rotational energy loss are in place.[1] Regions excluded by the spin-down limit correspond to shaded areas in Fig. 12.

Equatorial ellipticity values can be constrained below $\epsilon = 10^{-5}$ for sources in binary systems, such as the ones analyzed by this search located at 1 kpc emitting within the 150–300 Hz band. Constraints below $\epsilon = 10^{-4}$ can be set for sources located at 2 kpc emitting within the 75–150 Hz band. These sensitivities approach the expected allowed maximum ellipticities of relativisitic stars, which range from the order of $10^{-6}$–$10^{-7}$ to values around $10^{-5}$ for more exotic equations of state [47].

Future enhancements of the terrestrial gravitational wave detector network will improve our sensitivity to fainter gravitational wave signals, providing a valuable tool to prospect the expected population of galactic NSs in binary systems [48–52].

---

[1]An accretion-driven torque balance [43] could be subject to fluctuating accretion [44], leading to long-term phase wandering. This effect is unlikely to affect a semicoherent search like the one here reported, but it could have a significant impact during the follow-up stage, where longer coherence times are used [45,46].

## APPENDIX: FREQUENCY BANDS CONTAINING OUTLIERS

We provide a list of frequency bands in which outliers surviving the follow-up were found. These

TABLE VIII. Frequency bands containing line-crossing outliers. As described in Sec. VII C 1, these could be produced because of the presence of a transient instrumental artifact or the frequency evolution of a candidate drifting away from the spectral disturbance. Overlapping frequency bands were grouped together for the sake of simplicity. Outliers belonging to this category show at least one per-segment $\mathcal{F}$-statistic value greater than 100. Timestamps refer to the first and last coherent segments ($T_{\mathrm{coh}} \simeq 17$ h), for which, at least one of those candidates showed an $\mathcal{F}$-statistic value over 50. The last column relates these bands to the list of unidentified lines [31].

| Min. frequency [Hz] | Max. frequency [Hz] | First timestamp [GPS] | Last timestamp [GPS] | Duration [days] | Detector | Listed |
|---|---|---|---|---|---|---|
| 55.605 | 55.606 | 1239194624 | 1253831680 | 169 | H1 | Yes |
| 57.588 | 57.592 | 1243670016 | 1253770240 | 116 | H1 | Yes |
| 59.501 | 59.513 | 1238290944 | 1253831680 | 179 | H1 | Yes |
| 62.474 | 62.478 | 1244523008 | 1251895296 | 85 | H1 | Yes |
| 64.257 | 64.266 | 1241190400 | 1252681728 | 133 | H1 | No |
| 64.284 | 64.291 | 1238955520 | 1253831680 | 172 | H1 | Yes |
| 64.470 | 64.475 | 1239557632 | 1253770240 | 164 | H1 | Yes |
| 64.403 | 64.408 | 1240341504 | 1253588992 | 153 | H1 | Yes |
| 64.364 | 64.375 | 1238529536 | 1253831680 | 177 | H1 | Yes |
| 64.415 | 64.417 | 1239375872 | 1253831680 | 167 | H1 | Yes |
| 70.124 | 70.128 | 1238408192 | 1245484544 | 81 | H1 | Yes |
| 80.067 | 80.070 | 1238351360 | 1238351360 | 0 | H1 | No |
| 83.307 | 83.316 | 1238351360 | 1253831680 | 179 | H1 | Yes |
| 83.446 | 83.448 | 1238831616 | 1253831680 | 173 | H1 | Yes |
| 85.712 | 85.715 | 1239194624 | 1253831680 | 169 | H1 | Yes |
| 85.964 | 85.965 | 1239738880 | 1253165568 | 155 | H1 | Yes |
| 99.966 | 99.979 | 1238290944 | 1253831680 | 179 | H1 | Yes |
| 107.113 | 107.119 | 1241129984 | 1253709824 | 145 | H1 | Yes |
| 140.253 | 140.254 | 1238955520 | 1245424128 | 74 | H1 | Yes |
| 151.800 | 151.800 | 1253105152 | 1253105152 | 0 | H1 | Yes |
| 199.946 | 199.955 | 1242149888 | 1253770240 | 134 | H1 | Yes |
| 213.301 | 213.301 | 1242339840 | 1242339840 | 0 | L1 | Yes |

TABLE IX. Frequency bands containing outliers discarded by the detector consistency veto as described in Sec. VII C 2. Overlapping frequency bands were grouped together for the sake of simplicity. The last column relates these bands to the list of unidentified lines of the H1 detector [31].

| Min. frequency [Hz] | Max. frequency [Hz] | Listed |
|---|---|---|
| 53.709 | 53.721 | No |
| 55.603 | 55.609 | Yes |
| 57.583 | 57.600 | Yes |
| 62.823 | 62.828 | Yes |
| 64.400 | 64.411 | Yes |
| 83.442 | 83.453 | Yes |
| 85.815 | 85.824 | No |

outliers were discarded due to their inconsistent behavior with respect to an astrophysical signal, as discussed in Sec. VII. Table VIII lists frequency bands where line-crossing outliers were found. Table IX corresponds to frequency bands presenting outliers discarded by the detector consistency veto. In both tables, overlapping frequency bands are merged together for the sake of compactness.

[1] M. Sieniawska and M. Bejger, Universe **5**, 217 (2019).
[2] A. Arvanitaki and S. Dubovsky, Phys. Rev. D **83**, 044026 (2011).
[3] J. Aasi *et al.* (LIGO Scientific Collaboration), Classical Quantum Gravity **32**, 074001 (2015).
[4] F. Acernese *et al.*, Classical Quantum Gravity **32**, 024001 (2015).
[5] B. P. Abbott *et al.* (LIGO Scientific and Virgo Collaborations), Phys. Rev. D **99**, 122002 (2019).
[6] B. P. Abbott *et al.*, Astrophys. J. **879**, 10 (2019).
[7] B. P. Abbott *et al.* (LIGO Scientific and Virgo Collaborations), Phys. Rev. D **100**, 122002 (2019).
[8] B. P. Abbott *et al.* (LIGO Scientific and Virgo Collaborations), Phys. Rev. D **100**, 024004 (2019).
[9] R. Abbott *et al.* (LIGO Scientific and Virgo Collaborations), Astrophys. J. Lett. **902**, L21 (2020).
[10] R. Abbott *et al.* (LIGO Scientific, Virgo Collaboration, and KAGRA Collaborations), arXiv:2012.12926.
[11] P. R. Brady, T. Creighton, C. Cutler, and B. F. Schutz, Phys. Rev. D **57**, 2101 (1998).
[12] K. Rajwade, J. Chennamangalam, D. Lorimer, and A. Karastergiou, Mon. Not. R. Astron. Soc. **479**, 3094 (2018).
[13] P. B. Covas and A. M. Sintes, Phys. Rev. D **99**, 124019 (2019).
[14] R. N. Manchester, G. B. Hobbs, A. Teoh, and M. Hobbs, Astron. J. **129**, 1993 (2005).
[15] B. Krishnan, A. M. Sintes, M. A. Papa, B. F. Schutz, S. Frasca, and C. Palomba, Phys. Rev. D **70**, 082001 (2004).
[16] P. B. Covas and A. M. Sintes, Phys. Rev. Lett. **124**, 191102 (2020).
[17] P. Jaranowski and A. Królak, Phys. Rev. D **59**, 063003 (1999).
[18] P. Leaci and R. Prix, Phys. Rev. D **91**, 102003 (2015).
[19] A. Buikema *et al.*, Phys. Rev. D **102**, 062003 (2020).

[20] L. Sun *et al.*, Classical Quantum Gravity **37**, 225008 (2020).
[21] P. B. Covas *et al.* (LSC Instrument Authors), Phys. Rev. D **97**, 082002 (2018).
[22] A. Viets *et al.*, Classical Quantum Gravity **35**, 095015 (2018).
[23] P. Astone, S. Frasca, and C. Palomba, Classical Quantum Gravity **22**, S1197 (2005).
[24] M. Pitkin, J. Open Source Software **3**, 538 (2018).
[25] A. M. Sintes and B. Krishnan, J. Phys. Conf. Ser. **32**, 206 (2006).
[26] L. Sancho de la Jordana (LIGO Scientific and Virgo Collaborations), J. Phys. Conf. Ser. **228**, 012004 (2010).
[27] R. Tenorio, D. Keitel, and A. M. Sintes, arXiv:2012.05752.
[28] B. P. Abbott *et al.* (LIGO Scientific and Virgo Collaborations), Phys. Rev. D **96**, 062002 (2017).
[29] B. P. Abbott *et al.* (LIGO Scientific amd Virgo Collaboration), Phys. Rev. D **97**, 102003 (2018).
[30] E. Goetz, A. Neunzert, K. Riles, A. Mateas, S. Kandhasamy, J. Tasson *et al.* (LIGO Scientific Collaboration), O3a lines and combs in C00 data, https://dcc.ligo.org/T2000719/public (2020).
[31] E. Goetz, A. Neunzert, K. Riles, A. Mateas, S. Kandhasamy, J. Tasson *et al.* (LIGO Scientific Collaboration), Unidentified O3a lines and combs in C00 data, https://dcc.ligo.org/T2000720/public (2020).
[32] B. Behnke, M. A. Papa, and R. Prix, Phys. Rev. D **91**, 064007 (2015).
[33] C. Dreissigacker, R. Prix, and K. Wette, Phys. Rev. D **98**, 084058 (2018).
[34] B. P. Abbott *et al.* (LIGO Scientific and Virgo Collaborations), Phys. Rev. D **77**, 022001 (2008).
[35] P. Virtanen *et al.*, Nat. Methods **17**, 261 (2020).
[36] G. Ashton and R. Prix, Phys. Rev. D **97**, 103020 (2018).

[37] D. Keitel, R. Tenorio, G. Ashton, and R. Prix, arXiv:2101 .10915.

[38] G. Ashton, D. Keitel, R. Prix, and R. Tenorio, PyFstat v1.7.3 (2020), https://doi.org/10.5281/zenodo.4041983.

[39] LIGO Scientific Collaboration, LIGO Algorithm Library— LALSuite, https://doi.org/10.7935/GT1W-FZ16 (2018).

[40] D. Foreman-Mackey, D. W. Hogg, D. Lang, and J. Goodman, Publ. Astron. Soc. Pac. **125**, 306 (2013).

[41] W. D. Vousden, W. M. Farr, and I. Mandel, Mon. Not. R. Astron. Soc. **455**, 1919 (2016).

[42] D. Keitel, Phys. Rev. D **93**, 084024 (2016).

[43] L. Bildsten, Astrophys. J. Lett. **501**, L89 (1998).

[44] A. Watts, B. Krishnan, L. Bildsten, and B. F. Schutz, Mon. Not. R. Astron. Soc. **389**, 839 (2008).

[45] A. Mukherjee, C. Messenger, and K. Riles, Phys. Rev. D **97**, 043016 (2018).

[46] G. Ashton, R. Prix, and D. I. Jones, Phys. Rev. D **96**, 063004 (2017).

[47] N. K. Johnson-McDaniel and B. J. Owen, Phys. Rev. D **88**, 044004 (2013).

[48] T. Akutsu et al., Nat. Astron. **3**, 35 (2019).

[49] M. Maggiore et al., J. Cosmol. Astropart. Phys. 03 (2020) 050.

[50] D. Reitze et al., Bull. Am. Astron. Soc. **51**, 035 (2019), https://baas.aas.org/pub/2020n3i141/release/1.

[51] J. Miller, L. Barsotti, S. Vitale, P. Fritschel, M. Evans, and D. Sigg, Phys. Rev. D **91**, 062005 (2015).

[52] B. P. Abbott et al. (KAGRA, LIGO Scientific, and Virgo Collaborations), Living Rev. Relativity **23**, 3 (2020).

R. Abbott,[1] T. D. Abbott,[2] S. Abraham,[3] F. Acernese,[4,5] K. Ackley,[6] A. Adams,[7] C. Adams,[8] R. X. Adhikari,[1] V. B. Adya,[9] C. Affeldt,[10,11] D. Agarwal,[3] M. Agathos,[12,13] K. Agatsuma,[14] N. Aggarwal,[15] O. D. Aguiar,[16] L. Aiello,[17,18,19] A. Ain,[20,21] P. Ajith,[22] K. M. Aleman,[23] G. Allen,[24] A. Allocca,[25,5] P. A. Altin,[9] A. Amato,[26] S. Anand,[1] A. Ananyeva,[1] S. B. Anderson,[1] W. G. Anderson,[27] S. V. Angelova,[28] S. Ansoldi,[29,30] J. M. Antelis,[31] S. Antier,[32] S. Appert,[1] K. Arai,[1] M. C. Araya,[1] J. S. Areeda,[23] M. Arène,[32] N. Arnaud,[33,34] S. M. Aronson,[35] K. G. Arun,[36] Y. Asali,[37] G. Ashton,[6] S. M. Aston,[8] P. Astone,[38] F. Aubin,[39] P. Aufmuth,[10,11] K. AultONeal,[31] C. Austin,[2] S. Babak,[32] F. Badaracco,[18,19] M. K. M. Bader,[40] S. Bae,[41] A. M. Baer,[7] S. Bagnasco,[42] Y. Bai,[1] J. Baird,[32] M. Ball,[43] G. Ballardin,[34] S. W. Ballmer,[44] M. Bals,[31] A. Balsamo,[7] G. Baltus,[45] S. Banagiri,[46] D. Bankar,[3] R. S. Bankar,[3] J. C. Barayoga,[1] C. Barbieri,[47,48,49] B. C. Barish,[1] D. Barker,[50] P. Barneo,[51] S. Barnum,[52] F. Barone,[53,5] B. Barr,[54] L. Barsotti,[52] M. Barsuglia,[32] D. Barta,[55] J. Bartlett,[50] M. A. Barton,[54] I. Bartos,[35] R. Bassiri,[56] A. Basti,[21,20] M. Bawaj,[57,58] J. C. Bayley,[54] A. C. Baylor,[27] M. Bazzan,[59,60] B. Bécsy,[61] V. M. Bedakihale,[62] M. Bejger,[63] I. Belahcene,[33] V. Benedetto,[64] D. Beniwal,[65] M. G. Benjamin,[31] T. F. Bennett,[66] J. D. Bentley,[14] M. BenYaala,[28] F. Bergamin,[10,11] B. K. Berger,[56] S. Bernuzzi,[13] D. Bersanetti,[67] A. Bertolini,[40] J. Betzwieser,[8] R. Bhandare,[68] A. V. Bhandari,[3] D. Bhattacharjee,[69] S. Bhaumik,[35] J. Bidler,[23] I. A. Bilenko,[70] G. Billingsley,[1] R. Birney,[71] O. Birnholtz,[72] S. Biscans,[1,52] M. Bischi,[73,74] S. Biscoveanu,[52] A. Bisht,[10,11] B. Biswas,[3] M. Bitossi,[34,20] M.-A. Bizouard,[75] J. K. Blackburn,[1] J. Blackman,[76] C. D. Blair,[77,8] D. G. Blair,[77] R. M. Blair,[50] F. Bobba,[78,79] N. Bode,[10,11] M. Boer,[75] G. Bogaert,[75] M. Boldrini,[80,38] F. Bondu,[81] E. Bonilla,[56] R. Bonnand,[39] P. Booker,[10,11] B. A. Boom,[40] R. Bork,[1] V. Boschi,[20] N. Bose,[82] S. Bose,[3] V. Bossilkov,[77] V. Boudart,[45] Y. Bouffanais,[59,60] A. Bozzi,[34] C. Bradaschia,[20] P. R. Brady,[27] A. Bramley,[8] A. Branch,[8] M. Branchesi,[18,19] J. E. Brau,[43] M. Breschi,[13] T. Briant,[83] J. H. Briggs,[54] A. Brillet,[75] M. Brinkmann,[10,11] P. Brockill,[27] A. F. Brooks,[1] J. Brooks,[34] D. D. Brown,[65] S. Brunett,[1] G. Bruno,[84] R. Bruntz,[7] J. Bryant,[14] A. Buikema,[52] T. Bulik,[85] H. J. Bulten,[40,86] A. Buonanno,[87,88] R. Buscicchio,[14] D. Buskulic,[39] R. L. Byer,[56] L. Cadonati,[89] M. Caesar,[90] G. Cagnoli,[26] C. Cahillane,[1] H. W. Cain III,[2] J. Calderón Bustillo,[91] J. D. Callaghan,[54] T. A. Callister,[92,93] E. Calloni,[25,5] J. B. Camp,[94] M. Canepa,[95,67] M. Cannavacciuolo,[78] K. C. Cannon,[96] H. Cao,[65] J. Cao,[97] E. Capote,[23] G. Carapella,[78,79] F. Carbognani,[34] J. B. Carlin,[98] M. F. Carney,[15] M. Carpinelli,[99,100] G. Carullo,[21,20] T. L. Carver,[17] J. Casanueva Diaz,[34] C. Casentini,[101,102] G. Castaldi,[103] S. Caudill,[40,104] M. Cavaglià,[69] F. Cavalier,[33] R. Cavalieri,[34] G. Cella,[20] P. Cerdá-Durán,[105] E. Cesarini,[102] W. Chaibi,[75] K. Chakravarti,[3] B. Champion,[106] C.-H. Chan,[107] C. Chan,[96] C. L. Chan,[91] K. Chandra,[82] P. Chanial,[34] S. Chao,[107] P. Charlton,[108] E. A. Chase,[15] E. Chassande-Mottin,[32] D. Chatterjee,[27] M. Chaturvedi,[68] K. Chatziioannou,[1,92,93] A. Chen,[91] H. Y. Chen,[109] J. Chen,[107] X. Chen,[77] Y. Chen,[76] Z. Chen,[17] H. Cheng,[35] C. K. Cheong,[91] H. Y. Cheung,[91] H. Y. Chia,[35] F. Chiadini,[110,79] R. Chierici,[111] A. Chincarini,[67] M. L. Chiofalo,[21,20] A. Chiummo,[34] G. Cho,[112] H. S. Cho,[113] S. Choate,[90] R. K. Choudhary,[77] S. Choudhary,[3] N. Christensen,[75] Q. Chu,[77] S. Chua,[83] K. W. Chung,[114] G. Ciani,[59,60] P. Ciecielag,[63] M. Cieślar,[63] M. Cifaldi,[101,102] A. A. Ciobanu,[65] R. Ciolfi,[115,60] F. Cipriano,[75] A. Cirone,[95,67] F. Clara,[50] E. N. Clark,[116] J. A. Clark,[89] L. Clarke,[117] P. Clearwater,[98] S. Clesse,[118] F. Cleva,[75] E. Coccia,[18,19] P.-F. Cohadon,[83] D. E. Cohen,[33] L. Cohen,[2] M. Colleoni,[119] C. G. Collette,[120] M. Colpi,[47,48] C. M. Compton,[50] M. Constancio Jr.,[16] L. Conti,[60] S. J. Cooper,[14]

P. Corban,[8] T. R. Corbitt,[2] I. Cordero-Carrión,[121] S. Corezzi,[58,57] K. R. Corley,[37] N. Cornish,[61] D. Corre,[33] A. Corsi,[122] S. Cortese,[34] C. A. Costa,[16] R. Cotesta,[88] M. W. Coughlin,[46] S. B. Coughlin,[15,17] J.-P. Coulon,[75] S. T. Countryman,[37] B. Cousins,[123] P. Couvares,[1] P. B. Covas,[119] D. M. Coward,[77] M. J. Cowart,[8] D. C. Coyne,[1] R. Coyne,[124] J. D. E. Creighton,[27] T. D. Creighton,[125] A. W. Criswell,[46] M. Croquette,[83] S. G. Crowder,[126] J. R. Cudell,[45] T. J. Cullen,[2] A. Cumming,[54] R. Cummings,[54] E. Cuoco,[34,127,20] M. Curyło,[85] T. Dal Canton,[88,33] G. Dálya,[128] A. Dana,[56] L. M. DaneshgaranBajastani,[66] B. D'Angelo,[95,67] S. L. Danilishin,[129] S. D'Antonio,[102] K. Danzmann,[10,11] C. Darsow-Fromm,[130] A. Dasgupta,[62] L. E. H. Datrier,[54] V. Dattilo,[34] I. Dave,[68] M. Davier,[33] G. S. Davies,[131,132] D. Davis,[1] E. J. Daw,[133] R. Dean,[90] D. DeBra,[56] M. Deenadayalan,[3] J. Degallaix,[134] M. De Laurentis,[25,5] S. Deléglise,[83] V. Del Favero,[106] F. De Lillo,[84] N. De Lillo,[54] W. Del Pozzo,[21,20] L. M. DeMarchi,[15] F. De Matteis,[101,102] V. D'Emilio,[17] N. Demos,[52] T. Dent,[131] A. Depasse,[84] R. De Pietri,[135,136] R. De Rosa,[25,5] C. De Rossi,[34] R. DeSalvo,[103] R. De Simone,[110] S. Dhurandhar,[3] M. C. Díaz,[125] M. Diaz-Ortiz Jr.,[35] N. A. Didio,[44] T. Dietrich,[88] L. Di Fiore,[5] C. Di Fronzo,[14] C. Di Giorgio,[78,79] F. Di Giovanni,[105] T. Di Girolamo,[25,5] A. Di Lieto,[21,20] B. Ding,[120] S. Di Pace,[80,38] I. Di Palma,[80,38] F. Di Renzo,[21,20] A. K. Divakarla,[35] A. Dmitriev,[14] Z. Doctor,[43] L. D'Onofrio,[25,5] F. Donovan,[52] K. L. Dooley,[17] S. Doravari,[3] I. Dorrington,[17] M. Drago,[18,19] J. C. Driggers,[50] Y. Drori,[1] Z. Du,[97] J.-G. Ducoin,[33] P. Dupej,[54] O. Durante,[78,79] D. D'Urso,[99,100] P.-A. Duverne,[33] S. E. Dwyer,[50] P. J. Easter,[6] M. Ebersold,[137] G. Eddolls,[54] B. Edelman,[43] T. B. Edo,[1,133] O. Edy,[132] A. Effler,[8] J. Eichholz,[9] S. S. Eikenberry,[35] M. Eisenmann,[39] R. A. Eisenstein,[52] A. Ejlli,[17] L. Errico,[25,5] R. C. Essick,[109] H. Estellés,[119] D. Estevez,[138] Z. Etienne,[139] T. Etzel,[1] M. Evans,[52] T. M. Evans,[8] B. E. Ewing,[123] V. Fafone,[101,102,18] H. Fair,[44] S. Fairhurst,[17] X. Fan,[97] A. M. Farah,[109] S. Farinon,[67] B. Farr,[43] W. M. Farr,[92,93] N. W. Farrow,[6] E. J. Fauchon-Jones,[17] M. Favata,[140] M. Fays,[45,133] M. Fazio,[141] J. Feicht,[1] M. M. Fejer,[56] F. Feng,[32] E. Fenyvesi,[55,142] D. L. Ferguson,[89] A. Fernandez-Galiana,[52] I. Ferrante,[21,20] T. A. Ferreira,[16] F. Fidecaro,[21,20] P. Figura,[85] I. Fiori,[34] M. Fishbach,[15,109] R. P. Fisher,[7] J. M. Fishner,[52] R. Fittipaldi,[143,79] V. Fiumara,[144,79] R. Flaminio,[39,145] E. Floden,[46] E. Flynn,[23] H. Fong,[96] J. A. Font,[105,146] B. Fornal,[147] P. W. F. Forsyth,[9] A. Franke,[130] S. Frasca,[80,38] F. Frasconi,[20] C. Frederick,[148] Z. Frei,[128] A. Freise,[149] R. Frey,[43] V. V. Frolov,[8] G. G. Fronzé,[42] P. Fulda,[35] M. Fyffe,[8] H. A. Gabbard,[54] B. U. Gadre,[88] S. M. Gaebel,[14] J. R. Gair,[88] J. Gais,[91] S. Galaudage,[6] R. Gamba,[13] D. Ganapathy,[52] A. Ganguly,[22] S. G. Gaonkar,[3] B. Garaventa,[67,95] C. García-Núñez,[150] C. García-Quirós,[119] F. Garufi,[25,5] B. Gateley,[50] S. Gaudio,[31] V. Gayathri,[35] G. Gemme,[67] A. Gennai,[20] J. George,[68] L. Gergely,[151] P. Gewecke,[130] S. Ghonge,[89] Abhirup. Ghosh,[88] Archisman Ghosh,[152] Shaon Ghosh,[27,140] Shrobana Ghosh,[17] Sourath Ghosh,[35] B. Giacomazzo,[47,48,49] L. Giacoppo,[80,38] J. A. Giaime,[2,8] K. D. Giardina,[8] D. R. Gibson,[150] C. Gier,[28] M. Giesler,[76] P. Giri,[20,21] F. Gissi,[64] J. Glanzer,[2] A. E. Gleckl,[23] P. Godwin,[123] E. Goetz,[153] R. Goetz,[35] N. Gohlke,[10,11] B. Goncharov,[6] G. González,[2] A. Gopakumar,[154] M. Gosselin,[34] R. Gouaty,[39] B. Grace,[9] A. Grado,[155,5] M. Granata,[134] V. Granata,[78] A. Grant,[54] S. Gras,[52] P. Grassia,[1] C. Gray,[50] R. Gray,[54] G. Greco,[57] A. C. Green,[35] R. Green,[17] A. M. Gretarsson,[31] E. M. Gretarsson,[31] D. Griffith,[1] W. Griffiths,[17] H. L. Griggs,[89] G. Grignani,[58,57] A. Grimaldi,[156,157] E. Grimes,[31] S. J. Grimm,[18,19] H. Grote,[17] S. Grunewald,[88] P. Gruning,[33] J. G. Guerrero,[23] G. M. Guidi,[73,74] A. R. Guimaraes,[2] G. Guixé,[51] H. K. Gulati,[62] H.-K. Guo,[147] Y. Guo,[40] Anchal Gupta,[1] Anuradha Gupta,[158] P. Gupta,[40,104] E. K. Gustafson,[1] R. Gustafson,[159] F. Guzman,[116] L. Haegel,[32] O. Halim,[160,30] E. D. Hall,[52] E. Z. Hamilton,[17] G. Hammond,[54] M. Haney,[137] J. Hanks,[50] C. Hanna,[123] M. D. Hannam,[17] O. A. Hannuksela,[104,40,91] H. Hansen,[50] T. J. Hansen,[31] J. Hanson,[8] T. Harder,[75] T. Hardwick,[2] K. Haris,[40,104,22] J. Harms,[18,19] G. M. Harry,[161] I. W. Harry,[132] D. Hartwig,[130] B. Haskell,[63] R. K. Hasskew,[8] C.-J. Haster,[52] K. Haughian,[54] F. J. Hayes,[54] J. Healy,[106] A. Heidmann,[83] M. C. Heintze,[8] J. Heinze,[10,11] J. Heinzel,[162] H. Heitmann,[75] F. Hellman,[163] P. Hello,[33] A. F. Helmling-Cornell,[43] G. Hemming,[34] M. Hendry,[54] I. S. Heng,[54] E. Hennes,[40] J. Hennig,[10,11] M. H. Hennig,[10,11] F. Hernandez Vivanco,[6] M. Heurs,[10,11] S. Hild,[129,40] P. Hill,[28] A. S. Hines,[116] S. Hochheim,[10,11] D. Hofman,[134] J. N. Hohmann,[130] A. M. Holgado,[24] N. A. Holland,[9] I. J. Hollows,[133] Z. J. Holmes,[65] K. Holt,[8] D. E. Holz,[109] P. Hopkins,[17] J. Hough,[54] E. J. Howell,[77] C. G. Hoy,[17] D. Hoyland,[14] A. Hreibi,[10,11] Y. Hsu,[107] Y. Huang,[52] M. T. Hübner,[6] A. D. Huddart,[117] E. A. Huerta,[24] B. Hughey,[31] V. Hui,[39] S. Husa,[119] S. H. Huttner,[54] R. Huxford,[123] T. Huynh-Dinh,[8] B. Idzkowski,[85] A. Iess,[101,102] H. Inchauspe,[35] C. Ingram,[65] G. Intini,[80,38] M. Isi,[52] K. Isleif,[130] B. R. Iyer,[22] V. JaberianHamedan,[77] T. Jacqmin,[83] S. J. Jadhav,[164] S. P. Jadhav,[3] A. L. James,[17] A. Z. Jan,[106] K. Jani,[89] K. Janssens,[165] N. N. Janthalur,[164] P. Jaranowski,[166] D. Jariwala,[35] R. Jaume,[119] A. C. Jenkins,[114] M. Jeunon,[46] W. Jia,[52] J. Jiang,[35] G. R. Johns,[7] A. W. Jones,[77] D. I. Jones,[167] J. D. Jones,[50] P. Jones,[14] R. Jones,[54] R. J. G. Jonker,[40] L. Ju,[77] J. Junker,[10,11] C. V. Kalaghatgi,[17] V. Kalogera,[15] B. Kamai,[1] S. Kandhasamy,[3] G. Kang,[41] J. B. Kanner,[1] Y. Kao,[107] S. J. Kapadia,[22] D. P. Kapasi,[9] C. Karathanasis,[168] S. Karki,[69] R. Kashyap,[123] M. Kasprzack,[1] W. Kastaun,[10,11]

S. Katsanevas,[34] E. Katsavounidis,[52] W. Katzman,[8] T. Kaur,[77] K. Kawabe,[50] F. Kéfélian,[75] D. Keitel,[119] J. S. Key,[169] S. Khadka,[56] F. Y. Khalili,[70] I. Khan,[18,102] S. Khan,[17] E. A. Khazanov,[170] N. Khetan,[18,19] M. Khursheed,[68] N. Kijbunchoo,[9] C. Kim,[171] J. C. Kim,[172] K. Kim,[173] W. S. Kim,[174] Y.-M. Kim,[175] C. Kimball,[15] P. J. King,[50] M. Kinley-Hanlon,[54] R. Kirchhoff,[10,11] J. S. Kissel,[50] L. Kleybolte,[130] S. Klimenko,[35] A. M. Knee,[153] T. D. Knowles,[139] E. Knyazev,[52] P. Koch,[10,11] G. Koekoek,[40,129] S. Koley,[40] P. Kolitsidou,[17] M. Kolstein,[168] K. Komori,[52] V. Kondrashov,[1] A. Kontos,[176] N. Koper,[10,11] M. Korobko,[130] M. Kovalam,[77] D. B. Kozak,[1] V. Kringel,[10,11] N. V. Krishnendu,[10,11] A. Królak,[177,178] G. Kuehn,[10,11] F. Kuei,[107] A. Kumar,[164] P. Kumar,[179] Rahul Kumar,[50] Rakesh Kumar,[62] K. Kuns,[52] S. Kwang,[27] D. Laghi,[21,20] E. Lalande,[180] T. L. Lam,[91] A. Lamberts,[75,181] M. Landry,[50] B. B. Lane,[52] R. N. Lang,[52] J. Lange,[182,106] B. Lantz,[56] I. La Rosa,[39] A. Lartaux-Vollard,[33] P. D. Lasky,[6] M. Laxen,[8] A. Lazzarini,[1] C. Lazzaro,[59,60] P. Leaci,[80,38] S. Leavey,[10,11] Y. K. Lecoeuche,[50] H. M. Lee,[173] H. W. Lee,[172] J. Lee,[112] K. Lee,[56] J. Lehmann,[10,11] A. Lemaître,[183] E. Leon,[23] N. Leroy,[33] N. Letendre,[39] Y. Levin,[6] J. N. Leviton,[159] A. K. Y. Li,[1] B. Li,[107] J. Li,[15] T. G. F. Li,[91] X. Li,[76] F. Linde,[184,40] S. D. Linker,[66] J. N. Linley,[54] T. B. Littenberg,[185] J. Liu,[10,11] K. Liu,[107] X. Liu,[27] M. Llorens-Monteagudo,[105] R. K. L. Lo,[1] A. Lockwood,[186] M. L. Lollie,[2] L. T. London,[52] A. Longo,[187,188] D. Lopez,[137] M. Lorenzini,[101,102] V. Loriette,[189] M. Lormand,[8] G. Losurdo,[20] J. D. Lough,[10,11] C. O. Lousto,[106] G. Lovelace,[23] H. Lück,[10,11] D. Lumaca,[101,102] A. P. Lundgren,[132] R. Macas,[17] M. MacInnis,[52] D. M. Macleod,[17] I. A. O. MacMillan,[1] A. Macquet,[75] I. Magaña Hernandez,[27] F. Magaña-Sandoval,[35] C. Magazzù,[20] R. M. Magee,[123] R. Maggiore,[14] E. Majorana,[80,38] I. Maksimovic,[189] S. Maliakal,[1] A. Malik,[68] N. Man,[75] V. Mandic,[46] V. Mangano,[80,38] J. L. Mango,[190] G. L. Mansell,[50,52] M. Manske,[27] M. Mantovani,[34] M. Mapelli,[59,60] F. Marchesoni,[191,57] F. Marion,[39] Z. Mark,[76] S. Márka,[37] Z. Márka,[37] C. Markakis,[12] A. S. Markosyan,[56] A. Markowitz,[1] E. Maros,[1] A. Marquina,[121] S. Marsat,[32] F. Martelli,[73,74] I. W. Martin,[54] R. M. Martin,[140] M. Martinez,[168] V. Martinez,[26] K. Martinovic,[114] D. V. Martynov,[14] E. J. Marx,[52] H. Masalehdan,[130] K. Mason,[52] E. Massera,[133] A. Masserot,[39] T. J. Massinger,[52] M. Masso-Reid,[54] S. Mastrogiovanni,[32] A. Matas,[88] M. Mateu-Lucena,[119] F. Matichard,[1,52] M. Matiushechkina,[10,11] N. Mavalvala,[52] J. J. McCann,[77] R. McCarthy,[50] D. E. McClelland,[9] P. McClincy,[123] S. McCormick,[8] L. McCuller,[52] G. I. McGhee,[54] S. C. McGuire,[192] C. McIsaac,[132] J. McIver,[153] D. J. McManus,[9] T. McRae,[9] S. T. McWilliams,[139] D. Meacher,[27] M. Mehmet,[10,11] A. K. Mehta,[88] A. Melatos,[98] D. A. Melchor,[23] G. Mendell,[50] A. Menendez-Vazquez,[168] C. S. Menoni,[141] R. A. Mercer,[27] L. Mereni,[134] K. Merfeld,[43] E. L. Merilh,[50] J. D. Merritt,[43] M. Merzougui,[75] S. Meshkov,[1,a] C. Messenger,[54] C. Messick,[182] P. M. Meyers,[98] F. Meylahn,[10,11] A. Mhaske,[3] A. Miani,[156,157] H. Miao,[14] I. Michaloliakos,[35] C. Michel,[134] H. Middleton,[98] L. Milano,[25] A. L. Miller,[84,35] M. Millhouse,[98] J. C. Mills,[17] E. Milotti,[160,30] M. C. Milovich-Goff,[66] O. Minazzoli,[75,193] Y. Minenkov,[102] Ll. M. Mir,[168] A. Mishkin,[35] C. Mishra,[194] T. Mishra,[35] T. Mistry,[133] S. Mitra,[3] V. P. Mitrofanov,[70] G. Mitselmakher,[35] R. Mittleman,[52] Geoffrey Mo,[52] K. Mogushi,[69] S. R. P. Mohapatra,[52] S. R. Mohite,[27] I. Molina,[23] M. Molina-Ruiz,[163] M. Mondin,[66] M. Montani,[73,74] C. J. Moore,[14] D. Moraru,[50] F. Morawski,[63] A. More,[3] C. Moreno,[31] G. Moreno,[50] S. Morisaki,[96] B. Mours,[138] C. M. Mow-Lowry,[14] S. Mozzon,[132] F. Muciaccia,[80,38] Arunava Mukherjee,[195,54] D. Mukherjee,[123] Soma Mukherjee,[125] Subroto Mukherjee,[62] N. Mukund,[10,11] A. Mullavey,[8] J. Munch,[65] E. A. Muñiz,[44] P. G. Murray,[54] R. Musenich,[67,95] S. L. Nadji,[10,11] A. Nagar,[42,196] I. Nardecchia,[101,102] L. Naticchioni,[38] B. Nayak,[66] R. K. Nayak,[197] B. F. Neil,[77] J. Neilson,[64,79] G. Nelemans,[198] T. J. N. Nelson,[8] M. Nery,[10,11] A. Neunzert,[169] K. Y. Ng,[52] S. W. S. Ng,[65] C. Nguyen,[32] P. Nguyen,[43] T. Nguyen,[52] S. A. Nichols,[2] S. Nissanke,[199,40] F. Nocera,[34] M. Noh,[153] M. Norman,[17] C. North,[17] L. K. Nuttall,[132] J. Oberling,[50] B. D. O'Brien,[35] J. O'Dell,[117] G. Oganesyan,[18,19] J. J. Oh,[174] S. H. Oh,[174] F. Ohme,[10,11] H. Ohta,[96] M. A. Okada,[16] C. Olivetto,[34] R. Oram,[8] B. O'Reilly,[8] R. G. Ormiston,[46] N. D. Ormsby,[7] L. F. Ortega,[35] R. O'Shaughnessy,[106] E. O'Shea,[179] S. Ossokine,[88] C. Osthelder,[1] D. J. Ottaway,[65] H. Overmier,[8] A. E. Pace,[123] G. Pagano,[21,20] M. A. Page,[77] G. Pagliaroli,[18,19] A. Pai,[82] S. A. Pai,[68] J. R. Palamos,[43] O. Palashov,[170] C. Palomba,[38] P. K. Panda,[164] P. T. H. Pang,[40,104] C. Pankow,[15] F. Pannarale,[80,38] B. C. Pant,[68] F. Paoletti,[20] A. Paoli,[34] A. Paolone,[38,200] W. Parker,[8,192] D. Pascucci,[40] A. Pasqualetti,[34] R. Passaquieti,[21,20] D. Passuello,[20] M. Patel,[7] B. Patricelli,[34,20] E. Payne,[6] T. C. Pechsiri,[35] M. Pedraza,[1] M. Pegoraro,[60] A. Pele,[8] S. Penn,[201] A. Perego,[156,157] A. Pereira,[26] T. Pereira,[202] C. J. Perez,[50] C. Périgois,[39] A. Perreca,[156,157] S. Perriès,[111] J. Petermann,[130] D. Petterson,[1] H. P. Pfeiffer,[88] K. A. Pham,[46] K. S. Phukon,[40,184,3] O. J. Piccinni,[38] M. Pichot,[75] M. Piendibene,[21,20] F. Piergiovanni,[73,74] L. Pierini,[80,38] V. Pierro,[64,79] G. Pillant,[34] F. Pilo,[20] L. Pinard,[134] I. M. Pinto,[64,79,203] B. J. Piotrzkowski,[27] K. Piotrzkowski,[84] M. Pirello,[50] M. Pitkin,[204] E. Placidi,[80,38] W. Plastino,[187,188] C. Pluchar,[116] R. Poggiani,[21,20] E. Polini,[39] D. Y. T. Pong,[91] S. Ponrathnam,[3] P. Popolizio,[34] E. K. Porter,[32] J. Powell,[205] M. Pracchia,[39] T. Pradier,[138] A. K. Prajapati,[62] K. Prasai,[56] R. Prasanna,[164] G. Pratten,[14] T. Prestegard,[27] M. Principe,[64,203,79] G. A. Prodi,[206,157] L. Prokhorov,[14] P. Prosposito,[101,102] L. Prudenzi,[88]

A. Puecher,[40,104] M. Punturo,[57] F. Puosi,[20,21] P. Puppo,[38] M. Pürrer,[88] H. Qi,[17] V. Quetschke,[125] P. J. Quinonez,[31] R. Quitzow-James,[69] F. J. Raab,[50] G. Raaijmakers,[199,40] H. Radkins,[50] N. Radulesco,[75] P. Raffai,[128] S. X. Rail,[180] S. Raja,[68] C. Rajan,[68] K. E. Ramirez,[125] T. D. Ramirez,[23] A. Ramos-Buades,[88] J. Rana,[123] P. Rapagnani,[80,38] U. D. Rapol,[207] B. Ratto,[31] V. Raymond,[17] N. Raza,[153] M. Razzano,[21,20] J. Read,[23] L. A. Rees,[161] T. Regimbau,[39] L. Rei,[67] S. Reid,[28] D. H. Reitze,[1,35] P. Relton,[17] P. Rettegno,[208,42] F. Ricci,[80,38] C. J. Richardson,[31] J. W. Richardson,[1] L. Richardson,[116] P. M. Ricker,[24] G. Riemenschneider,[208,42] K. Riles,[159] M. Rizzo,[15] N. A. Robertson,[1,54] R. Robie,[1] F. Robinet,[33] A. Rocchi,[102] J. A. Rocha,[23] S. Rodriguez,[23] R. D. Rodriguez-Soto,[31] L. Rolland,[39] J. G. Rollins,[1] V. J. Roma,[43] M. Romanelli,[81] R. Romano,[4,5] C. L. Romel,[50] A. Romero,[168] I. M. Romero-Shaw,[6] J. H. Romie,[8] C. A. Rose,[27] D. Rosińska,[85] S. G. Rosofsky,[24] M. P. Ross,[186] S. Rowan,[54] S. J. Rowlinson,[14] Santosh Roy,[3] Soumen Roy,[209] D. Rozza,[99,100] P. Ruggi,[34] K. Ryan,[50] S. Sachdev,[123] T. Sadecki,[50] J. Sadiq,[131] M. Sakellariadou,[114] O. S. Salafia,[49,48,47] L. Salconi,[34] M. Saleem,[36] F. Salemi,[156,157] A. Samajdar,[40,104] E. J. Sanchez,[1] J. H. Sanchez,[23] L. E. Sanchez,[1] N. Sanchis-Gual,[210] J. R. Sanders,[211] A. Sanuy,[51] T. R. Saravanan,[3] N. Sarin,[6] B. Sassolas,[134] H. Satari,[77] O. Sauter,[35,39] R. L. Savage,[50] V. Savant,[3] D. Sawant,[82] H. L. Sawant,[3] S. Sayah,[134] D. Schaetzl,[1] M. Scheel,[76] J. Scheuer,[15] A. Schindler-Tyka,[35] P. Schmidt,[14] R. Schnabel,[130] M. Schneewind,[10,11] R. M. S. Schofield,[43] A. Schönbeck,[130] B. W. Schulte,[10,11] B. F. Schutz,[17,10] E. Schwartz,[17] J. Scott,[54] S. M. Scott,[9] M. Seglar-Arroyo,[39] E. Seidel,[24] D. Sellers,[8] A. Sergeev,[170] A. S. Sengupta,[209] N. Sennett,[88] D. Sentenac,[34] E. G. Seo,[91] V. Sequino,[25,5] Y. Setyawati,[10,11] T. Shaffer,[50] M. S. Shahriar,[15] B. Shams,[147] S. Sharifi,[2] A. Sharma,[18,19] P. Sharma,[68] P. Shawhan,[87] N. S. Shcheblanov,[183] H. Shen,[24] M. Shikauchi,[96] R. Shink,[180] D. H. Shoemaker,[52] D. M. Shoemaker,[182] K. Shukla,[163] S. ShyamSundar,[68] M. Sieniawska,[85] D. Sigg,[50] L. P. Singer,[94] D. Singh,[123] N. Singh,[85] A. Singha,[129,40] A. M. Sintes,[119] V. Sipala,[99,100] V. Skliris,[17] B. J. J. Slagmolen,[9] T. J. Slaven-Blair,[77] J. Smetana,[14] J. R. Smith,[23] R. J. E. Smith,[6] S. N. Somala,[212] E. J. Son,[174] K. Soni,[3] S. Soni,[2] B. Sorazu,[54] V. Sordini,[111] F. Sorrentino,[67] N. Sorrentino,[21,20] R. Soulard,[75] T. Souradeep,[207,3] E. Sowell,[122] V. Spagnuolo,[129,40] A. P. Spencer,[54] M. Spera,[59,60] A. K. Srivastava,[62] V. Srivastava,[44] K. Staats,[15] C. Stachie,[75] D. A. Steer,[32] J. Steinlechner,[129,40] S. Steinlechner,[129,40] D. J. Stops,[14] M. Stover,[148] K. A. Strain,[54] L. C. Strang,[98] G. Stratta,[213,74] A. Strunk,[50] R. Sturani,[202] A. L. Stuver,[90] J. Südbeck,[130] S. Sudhagar,[3] V. Sudhir,[52] H. G. Suh,[27] T. Z. Summerscales,[214] H. Sun,[77] L. Sun,[9,1] S. Sunil,[62] A. Sur,[63] J. Suresh,[96] P. J. Sutton,[17] B. L. Swinkels,[40] M. J. Szczepańczyk,[35] P. Szewczyk,[85] M. Tacca,[40] S. C. Tait,[54] C. Talbot,[1] A. J. Tanasijczuk,[84] D. B. Tanner,[35] D. Tao,[1] A. Tapia,[23] E. N. Tapia San Martin,[40] J. D. Tasson,[162] R. Tenorio,[119] L. Terkowski,[130] M. Test,[27] M. P. Thirugnanasambandam,[3] M. Thomas,[8] P. Thomas,[50] J. E. Thompson,[17] S. R. Thondapu,[68] K. A. Thorne,[8] E. Thrane,[6] Shubhanshu Tiwari,[137] Srishti Tiwari,[154] V. Tiwari,[17] K. Toland,[54] A. E. Tolley,[132] M. Tonelli,[21,20] A. Torres-Forné,[105] C. I. Torrie,[1] I. Tosta e Melo,[99,100] D. Töyrä,[9] A. Trapananti,[191,57] F. Travasso,[57,191] G. Traylor,[8] M. C. Tringali,[34] A. Tripathee,[159] L. Troiano,[215,79] A. Trovato,[32] R. J. Trudeau,[1] D. S. Tsai,[107] D. Tsai,[107] K. W. Tsang,[40,216,104] M. Tse,[52] R. Tso,[76] L. Tsukada,[96] D. Tsuna,[96] T. Tsutsui,[96] M. Turconi,[75] A. S. Ubhi,[14] R. P. Udall,[89,1] K. Ueno,[96] D. Ugolini,[217] C. S. Unnikrishnan,[154] A. L. Urban,[2] S. A. Usman,[109] A. C. Utina,[129,40] H. Vahlbruch,[10,11] G. Vajente,[1] A. Vajpeyi,[6] G. Valdes,[2] M. Valentini,[156,157] V. Valsan,[27] N. van Bakel,[40] M. van Beuzekom,[40] J. F. J. van den Brand,[129,86,40] C. Van Den Broeck,[104,40] D. C. Vander-Hyde,[44] L. van der Schaaf,[40] J. V. van Heijningen,[77,84] M. Vardaro,[184,40] A. F. Vargas,[98] V. Varma,[76] M. Vasúth,[218] A. Vecchio,[14] G. Vedovato,[60] J. Veitch,[54] P. J. Veitch,[65] K. Venkateswara,[186] J. Venneberg,[10,11] G. Venugopalan,[1] D. Verkindt,[39] Y. Verma,[68] D. Veske,[37] F. Vetrano,[73] A. Viceré,[73,74] A. D. Viets,[190] V. Villa-Ortega,[131] J.-Y. Vinet,[75] S. Vitale,[52] T. Vo,[44] H. Vocca,[58,57] E. R. G. von Reis,[50] J. von Wrangel,[10,11] C. Vorvick,[50] S. P. Vyatchanin,[70] L. E. Wade,[148] M. Wade,[148] K. J. Wagner,[106] R. C. Walet,[40] M. Walker,[7] G. S. Wallace,[28] L. Wallace,[1] S. Walsh,[27] J. Z. Wang,[159] W. H. Wang,[125] R. L. Ward,[9] J. Warner,[50] M. Was,[39] N. Y. Washington,[1] J. Watchi,[120] B. Weaver,[50] L. Wei,[10,11] M. Weinert,[10,11] A. J. Weinstein,[1] R. Weiss,[52] C. M. Weller,[186] F. Wellmann,[10,11] L. Wen,[77] P. Weßels,[10,11] J. W. Westhouse,[31] K. Wette,[9] J. T. Whelan,[106] D. D. White,[23] B. F. Whiting,[35] C. Whittle,[52] D. Wilken,[10,11] D. Williams,[54] M. J. Williams,[54] A. R. Williamson,[132] J. L. Willis,[1] B. Willke,[10,11] D. J. Wilson,[116] W. Winkler,[10,11] C. C. Wipf,[1] T. Wlodarczyk,[88] G. Woan,[54] J. Woehler,[10,11] J. K. Wofford,[106] I. C. F. Wong,[91] D. S. Wu,[10,11] D. M. Wysocki,[27,106] L. Xiao,[1] H. Yamamoto,[1] F. W. Yang,[147] L. Yang,[141] Y. Yang,[35] Z. Yang,[46] M. J. Yap,[9] D. W. Yeeles,[17] A. B. Yelikar,[106] M. Ying,[107] A. Yoon,[7] Hang Yu,[76] Haocun Yu,[52] A. Zadrożny,[178] M. Zanolin,[31] T. Zelenova,[34] J.-P. Zendri,[60] M. Zevin,[15] J. Zhang,[77] L. Zhang,[1] R. Zhang,[35] T. Zhang,[14] C. Zhao,[77] G. Zhao,[120] Y. Zhao,[147] Z. Zhou,[15] X. J. Zhu,[6] M. E. Zucker,[1,52] and J. Zweizig[1]

(The LIGO Scientific Collaboration and the Virgo Collaboration)

[1]LIGO Laboratory, California Institute of Technology, Pasadena, California 91125, USA
[2]Louisiana State University, Baton Rouge, Louisiana 70803, USA
[3]Inter-University Centre for Astronomy and Astrophysics, Pune 411007, India
[4]Dipartimento di Farmacia, Università di Salerno, I-84084 Fisciano, Salerno, Italy
[5]INFN, Sezione di Napoli, Complesso Universitario di Monte S.Angelo, I-80126 Napoli, Italy
[6]OzGrav, School of Physics & Astronomy, Monash University, Clayton 3800, Victoria, Australia
[7]Christopher Newport University, Newport News, Virginia 23606, USA
[8]LIGO Livingston Observatory, Livingston, Louisiana 70754, USA
[9]OzGrav, Australian National University, Canberra, Australian Capital Territory 0200, Australia
[10]Max Planck Institute for Gravitational Physics (Albert Einstein Institute), D-30167 Hannover, Germany
[11]Leibniz Universität Hannover, D-30167 Hannover, Germany
[12]University of Cambridge, Cambridge CB2 1TN, United Kingdom
[13]Theoretisch-Physikalisches Institut, Friedrich-Schiller-Universität Jena, D-07743 Jena, Germany
[14]University of Birmingham, Birmingham B15 2TT, United Kingdom
[15]Center for Interdisciplinary Exploration & Research in Astrophysics (CIERA), Northwestern University,
Evanston, Illinois 60208, USA
[16]Instituto Nacional de Pesquisas Espaciais, 12227-010 São José dos Campos, São Paulo, Brazil
[17]Gravity Exploration Institute, Cardiff University, Cardiff CF24 3AA, United Kingdom
[18]Gran Sasso Science Institute (GSSI), I-67100 L'Aquila, Italy
[19]INFN, Laboratori Nazionali del Gran Sasso, I-67100 Assergi, Italy
[20]INFN, Sezione di Pisa, I-56127 Pisa, Italy
[21]Università di Pisa, I-56127 Pisa, Italy
[22]International Centre for Theoretical Sciences, Tata Institute of Fundamental Research,
Bengaluru 560089, India
[23]California State University Fullerton, Fullerton, California 92831, USA
[24]NCSA, University of Illinois at Urbana-Champaign, Urbana, Illinois 61801, USA
[25]Università di Napoli "Federico II", Complesso Universitario di Monte S.Angelo, I-80126 Napoli, Italy
[26]Université de Lyon, Université Claude Bernard Lyon 1, CNRS, Institut Lumière Matière,
F-69622 Villeurbanne, France
[27]University of Wisconsin-Milwaukee, Milwaukee, Wisconsin 53201, USA
[28]SUPA, University of Strathclyde, Glasgow G1 1XQ, United Kingdom
[29]Dipartimento di Matematica e Informatica, Università di Udine, I-33100 Udine, Italy
[30]INFN, Sezione di Trieste, I-34127 Trieste, Italy
[31]Embry-Riddle Aeronautical University, Prescott, Arizona 86301, USA
[32]Université de Paris, CNRS, Astroparticule et Cosmologie, F-75006 Paris, France
[33]Université Paris-Saclay, CNRS/IN2P3, IJCLab, 91405 Orsay, France
[34]European Gravitational Observatory (EGO), I-56021 Cascina, Pisa, Italy
[35]University of Florida, Gainesville, Florida 32611, USA
[36]Chennai Mathematical Institute, Chennai 603103, India
[37]Columbia University, New York, New York 10027, USA
[38]INFN, Sezione di Roma, I-00185 Roma, Italy
[39]Laboratoire d'Annecy de Physique des Particules (LAPP), Univ. Grenoble Alpes,
Université Savoie Mont Blanc, CNRS/IN2P3, F-74941 Annecy, France
[40]Nikhef, Science Park 105, 1098 XG Amsterdam, Netherlands
[41]Korea Institute of Science and Technology Information, Daejeon 34141, South Korea
[42]INFN Sezione di Torino, I-10125 Torino, Italy
[43]University of Oregon, Eugene, Oregon 97403, USA
[44]Syracuse University, Syracuse, New York 13244, USA
[45]Université de Liège, B-4000 Liège, Belgium
[46]University of Minnesota, Minneapolis, Minnesota 55455, USA
[47]Università degli Studi di Milano-Bicocca, I-20126 Milano, Italy
[48]INFN, Sezione di Milano-Bicocca, I-20126 Milano, Italy
[49]INAF, Osservatorio Astronomico di Brera sede di Merate, I-23807 Merate, Lecco, Italy
[50]LIGO Hanford Observatory, Richland, Washington 99352, USA
[51]Institut de Ciències del Cosmos, Universitat de Barcelona,
C/ Martí i Franquès 1, Barcelona, 08028, Spain
[52]LIGO Laboratory, Massachusetts Institute of Technology, Cambridge, Massachusetts 02139, USA
[53]Dipartimento di Medicina, Chirurgia e Odontoiatria "Scuola Medica Salernitana",
Università di Salerno, I-84081 Baronissi, Salerno, Italy

[54]SUPA, University of Glasgow, Glasgow G12 8QQ, United Kingdom

[55]Wigner RCP, RMKI, H-1121 Budapest, Konkoly Thege Miklós út 29-33, Hungary

[56]Stanford University, Stanford, California 94305, USA

[57]INFN, Sezione di Perugia, I-06123 Perugia, Italy

[58]Università di Perugia, I-06123 Perugia, Italy

[59]Università di Padova, Dipartimento di Fisica e Astronomia, I-35131 Padova, Italy

[60]INFN, Sezione di Padova, I-35131 Padova, Italy

[61]Montana State University, Bozeman, Montana 59717, USA

[62]Institute for Plasma Research, Bhat, Gandhinagar 382428, India

[63]Nicolaus Copernicus Astronomical Center, Polish Academy of Sciences, 00-716, Warsaw, Poland

[64]Dipartimento di Ingegneria, Università del Sannio, I-82100 Benevento, Italy

[65]OzGrav, University of Adelaide, Adelaide, South Australia 5005, Australia

[66]California State University, Los Angeles, 5151 State University Dr, Los Angeles, California 90032, USA

[67]INFN, Sezione di Genova, I-16146 Genova, Italy

[68]RRCAT, Indore, Madhya Pradesh 452013, India

[69]Missouri University of Science and Technology, Rolla, Missouri 65409, USA

[70]Faculty of Physics, Lomonosov Moscow State University, Moscow 119991, Russia

[71]SUPA, University of the West of Scotland, Paisley PA1 2BE, United Kingdom

[72]Bar-Ilan University, Ramat Gan, 5290002, Israel

[73]Università degli Studi di Urbino "Carlo Bo", I-61029 Urbino, Italy

[74]INFN, Sezione di Firenze, I-50019 Sesto Fiorentino, Firenze, Italy

[75]Artemis, Université Côte d'Azur, Observatoire de Louisiana Côte d'Azur, CNRS, F-06304 Nice, France

[76]CaRT, California Institute of Technology, Pasadena, California 91125, USA

[77]OzGrav, University of Western Australia, Crawley, Western Australia 6009, Australia

[78]Dipartimento di Fisica "E.R. Caianiello", Università di Salerno, I-84084 Fisciano, Salerno, Italy

[79]INFN, Sezione di Napoli, Gruppo Collegato di Salerno, Complesso Universitario di Monte S. Angelo, I-80126 Napoli, Italy

[80]Università di Roma "Louisiana Sapienza", I-00185 Roma, Italy

[81]Univ Rennes, CNRS, Institut FOTON—UMR6082, F-3500 Rennes, France

[82]Indian Institute of Technology Bombay, Powai, Mumbai 400 076, India

[83]Laboratoire Kastler Brossel, Sorbonne Université, CNRS, ENS-Université PSL, Collège de France, F-75005 Paris, France

[84]Université catholique de Louvain, B-1348 Louvain-Louisiana-Neuve, Belgium

[85]Astronomical Observatory Warsaw University, 00-478 Warsaw, Poland

[86]VU University Amsterdam, 1081 HV Amsterdam, Netherlands

[87]University of Maryland, College Park, Maryland 20742, USA

[88]Max Planck Institute for Gravitational Physics (Albert Einstein Institute), D-14476 Potsdam, Germany

[89]School of Physics, Georgia Institute of Technology, Atlanta, Georgia 30332, USA

[90]Villanova University, 800 Lancaster Ave, Villanova, Pennsylvania 19085, USA

[91]The Chinese University of Hong Kong, Shatin, NT, Hong Kong

[92]Stony Brook University, Stony Brook, New York 11794, USA

[93]Center for Computational Astrophysics, Flatiron Institute, New York, New York 10010, USA

[94]NASA Goddard Space Flight Center, Greenbelt, Maryland 20771, USA

[95]Dipartimento di Fisica, Università degli Studi di Genova, I-16146 Genova, Italy

[96]RESCEU, University of Tokyo, Tokyo, 113-0033, Japan.

[97]Tsinghua University, Beijing 100084, China

[98]OzGrav, University of Melbourne, Parkville, Victoria 3010, Australia

[99]Università degli Studi di Sassari, I-07100 Sassari, Italy

[100]INFN, Laboratori Nazionali del Sud, I-95125 Catania, Italy

[101]Università di Roma Tor Vergata, I-00133 Roma, Italy

[102]INFN, Sezione di Roma Tor Vergata, I-00133 Roma, Italy

[103]University of Sannio at Benevento, I-82100 Benevento, Italy and INFN, Sezione di Napoli, I-80100 Napoli, Italy

[104]Institute for Gravitational and Subatomic Physics (GRASP), Utrecht University, Princetonplein 1, 3584 CC Utrecht, Netherlands

[105]Departamento de Astronomía y Astrofísica, Universitat de València, E-46100 Burjassot, València, Spain

[106]Rochester Institute of Technology, Rochester, New York 14623, USA

[107]National Tsing Hua University, Hsinchu City, 30013 Taiwan, Republic of China

[108]OzGrav, Charles Sturt University, Wagga Wagga, New South Wales 2678, Australia

[109]University of Chicago, Chicago, Illinois 60637, USA

[110]Dipartimento di Ingegneria Industriale (DIIN), Università di Salerno, I-84084 Fisciano, Salerno, Italy

[111]Institut de Physique des 2 Infinis de Lyon (IP2I), CNRS/IN2P3, Université de Lyon,
Université Claude Bernard Lyon 1, F-69622 Villeurbanne, France

[112]Seoul National University, Seoul 08826, South Korea

[113]Pusan National University, Busan 46241, South Korea

[114]King's College London, University of London, London WC2R 2LS, United Kingdom

[115]INAF, Osservatorio Astronomico di Padova, I-35122 Padova, Italy

[116]University of Arizona, Tucson, Arizona 85721, USA

[117]Rutherford Appleton Laboratory, Didcot OX11 0DE, United Kingdom

[118]Université libre de Bruxelles, Avenue Franklin Roosevelt 50—1050 Bruxelles, Belgium

[119]Universitat de les Illes Balears, IAC3—IEEC, E-07122 Palma de Mallorca, Spain

[120]Université Libre de Bruxelles, Brussels 1050, Belgium

[121]Departamento de Matemáticas, Universitat de València, E-46100 Burjassot, València, Spain

[122]Texas Tech University, Lubbock, Texas 79409, USA

[123]The Pennsylvania State University, University Park, Pennsylvania 16802, USA

[124]University of Rhode Island, Kingston, Rhode Island 02881, USA

[125]The University of Texas Rio Grande Valley, Brownsville, Texas 78520, USA

[126]Bellevue College, Bellevue, Washington 98007, USA

[127]Scuola Normale Superiore, Piazza dei Cavalieri, 7—56126 Pisa, Italy

[128]MTA-ELTE Astrophysics Research Group, Institute of Physics, Eötvös University,
Budapest 1117, Hungary

[129]Maastricht University, 6200 Maryland, Maastricht, Netherlands

[130]Universität Hamburg, D-22761 Hamburg, Germany

[131]IGFAE, Campus Sur, Universidade de Santiago de Compostela, 15782 Spain

[132]University of Portsmouth, Portsmouth, PO1 3FX, United Kingdom

[133]The University of Sheffield, Sheffield S10 2TN, United Kingdom

[134]Laboratoire des Matériaux Avancés (LMA), Institut de Physique des 2 Infinis (IP2I) de Lyon, CNRS/
IN2P3, Université de Lyon, Université Claude Bernard Lyon 1, F-69622 Villeurbanne, France

[135]Dipartimento di Scienze Matematiche, Fisiche e Informatiche, Università di Parma,
I-43124 Parma, Italy

[136]INFN, Sezione di Milano Bicocca, Gruppo Collegato di Parma, I-43124 Parma, Italy

[137]Physik-Institut, University of Zurich, Winterthurerstrasse 190, 8057 Zurich, Switzerland

[138]Université de Strasbourg, CNRS, IPHC UMR 7178, F-67000 Strasbourg, France

[139]West Virginia University, Morgantown, West Virginia 26506, USA

[140]Montclair State University, Montclair, New Jersey 07043, USA

[141]Colorado State University, Fort Collins, Colorado 80523, USA

[142]Institute for Nuclear Research, Hungarian Academy of Sciences,
Bem t'er 18/c, H-4026 Debrecen, Hungary

[143]CNR-SPIN, c/o Università di Salerno, I-84084 Fisciano, Salerno, Italy

[144]Scuola di Ingegneria, Università della Basilicata, I-85100 Potenza, Italy

[145]Gravitational Wave Science Project, National Astronomical Observatory of Japan (NAOJ),
Mitaka City, Tokyo 181-8588, Japan

[146]Observatori Astronòmic, Universitat de València, E-46980 Paterna, València, Spain

[147]The University of Utah, Salt Lake City, Utah 84112, USA

[148]Kenyon College, Gambier, Ohio 43022, USA

[149]Vrije Universiteit Amsterdam, 1081 HV, Amsterdam, Netherlands

[150]SUPA, University of the West of Scotland, Paisley Pennsylvania1 2BE, United Kingdom

[151]University of Szeged, Dóm tér 9, Szeged 6720, Hungary

[152]Universiteit Gent, B-9000 Gent, Belgium

[153]University of British Columbia, Vancouver, BC V6T 1Z4, Canada

[154]Tata Institute of Fundamental Research, Mumbai 400005, India

[155]INAF, Osservatorio Astronomico di Capodimonte, I-80131 Napoli, Italy

[156]Università di Trento, Dipartimento di Fisica, I-38123 Povo, Trento, Italy

[157]INFN, Trento Institute for Fundamental Physics and Applications, I-38123 Povo, Trento, Italy

[158]The University of Mississippi, University, Mississippi 38677, USA

[159]University of Michigan, Ann Arbor, Michigan 48109, USA

[160]Dipartimento di Fisica, Università di Trieste, I-34127 Trieste, Italy

[161]American University, Washington, D.C. 20016, USA

[162]Carleton College, Northfield, Minnesota 55057, USA

[163]University of California, Berkeley, California 94720, USA

[164]Directorate of Construction, Services & Estate Management, Mumbai 400094 India

[165]Universiteit Antwerpen, Prinsstraat 13, 2000 Antwerpen, Belgium

[166]University of Białystok, 15-424 Białystok, Poland

[167]University of Southampton, Southampton SO17 1BJ, United Kingdom

[168]Institut de Física d'Altes Energies (IFAE), Barcelona Institute of Science and Technology, and ICREA,
E-08193 Barcelona, Spain

[169]University of Washington Bothell, Bothell, Washington 98011, USA

[170]Institute of Applied Physics, Nizhny Novgorod, 603950, Russia

[171]Ewha Womans University, Seoul 03760, South Korea

[172]Inje University Gimhae, South Gyeongsang 50834, South Korea

[173]Korea Astronomy and Space Science Institute, Daejeon 34055, South Korea

[174]National Institute for Mathematical Sciences, Daejeon 34047, South Korea

[175]Ulsan National Institute of Science and Technology, Ulsan 44919, South Korea

[176]Bard College, 30 Campus Rd, Annandale-On-Hudson, New York 12504, USA

[177]Institute of Mathematics, Polish Academy of Sciences, 00656 Warsaw, Poland

[178]National Center for Nuclear Research, 05-400 Świerk-Otwock, Poland

[179]Cornell University, Ithaca, New York 14850, USA

[180]Université de Montréal/Polytechnique, Montreal, Quebec H3T 1J4, Canada

[181]Laboratoire Lagrange, Université Côte d'Azur, Observatoire Côte d'Azur,
CNRS, F-06304 Nice, France

[182]Department of Physics, University of Texas, Austin, Texas 78712, USA

[183]NAVIER, École des Ponts, Univ Gustave Eiffel, CNRS, Marne-Louisiana-Vallée, France

[184]Institute for High-Energy Physics, University of Amsterdam,
Science Park 904, 1098 XH Amsterdam, Netherlands

[185]NASA Marshall Space Flight Center, Huntsville, Alabama 35811, USA

[186]University of Washington, Seattle, Washington 98195, USA

[187]Dipartimento di Matematica e Fisica, Università degli Studi Roma Tre, I-00146 Roma, Italy

[188]INFN, Sezione di Roma Tre, I-00146 Roma, Italy

[189]ESPCI, CNRS, F-75005 Paris, France

[190]Concordia University Wisconsin, Mequon, Wisconsin 53097, USA

[191]Università di Camerino, Dipartimento di Fisica, I-62032 Camerino, Italy

[192]Southern University and A&M College, Baton Rouge, Louisiana 70813, USA

[193]Centre Scientifique de Monaco, 8 quai Antoine Ier, MC-98000, Monaco

[194]Indian Institute of Technology Madras, Chennai 600036, India

[195]Saha Institute of Nuclear Physics, Bidhannagar, West Bengal 700064, India

[196]Institut des Hautes Etudes Scientifiques, F-91440 Bures-sur-Yvette, France

[197]Indian Institute of Science Education and Research, Kolkata, Mohanpur, West Bengal 741252, India

[198]Department of Astrophysics/IMAPP, Radboud University Nijmegen,
P.O. Box 9010, 6500 GL Nijmegen, Netherlands

[199]GRAPPA, Anton Pannekoek Institute for Astronomy and Institute for High-Energy Physics,
University of Amsterdam, Science Park 904, 1098 XH Amsterdam, Netherlands

[200]Consiglio Nazionale delle Ricerche—Istituto dei Sistemi Complessi,
Piazzale Aldo Moro 5, I-00185 Roma, Italy

[201]Hobart and William Smith Colleges, Geneva, New York 14456, USA

[202]International Institute of Physics, Universidade Federal do Rio Grande do Norte,
Natal RN 59078-970, Brazil

[203]Museo Storico della Fisica e Centro Studi e Ricerche "Enrico Fermi", I-00184 Roma, Italy

[204]Lancaster University, Lancaster Louisiana1 4YW, United Kingdom

[205]OzGrav, Swinburne University of Technology, Hawthorn VIC 3122, Australia

[206]Università di Trento, Dipartimento di Matematica, I-38123 Povo, Trento, Italy

[207]Indian Institute of Science Education and Research, Pune, Maharashtra 411008, India

[208]Dipartimento di Fisica, Università degli Studi di Torino, I-10125 Torino, Italy

[209]Indian Institute of Technology, Palaj, Gandhinagar, Gujarat 382355, India

[210]Centro de Astrofísica e Gravitação (CENTRA), Departamento de Física, Instituto Superior Técnico,
Universidade de Lisboa, 1049-001 Lisboa, Portugal

[211]Marquette University, 11420 W. Clybourn St., Milwaukee, Wisconsin 53233, USA

[212]Indian Institute of Technology Hyderabad, Sangareddy, Khandi, Telangana 502285, India

[213]INAF, Osservatorio di Astrofisica e Scienza dello Spazio, I-40129 Bologna, Italy

[214]*Andrews University, Berrien Springs, Michigan 49104, USA*

[215]*Dipartimento di Scienze Aziendali—Management and Innovation Systems (DISA-MIS),
Università di Salerno, I-84084 Fisciano, Salerno, Italy*

[216]*Van Swinderen Institute for Particle Physics and Gravity, University of Groningen,
Nijenborgh 4, 9747 AG Groningen, Netherlands*

[217]*Trinity University, San Antonio, Texas 78212, USA*

[218]*Wigner RCP, RMKI, H-1121 Budapest, Konkoly Thege Miklós Útah 29-33, Hungary*

[a]Deceased, August 2020.